Full length article

High water contents of magmas and extensive fluid exsolution during the formation of the Yulong porphyry Cu-Mo deposit, eastern Tibet

Ming-Liang Huang[a,b,c], Xian-Wu Bi[a,*], Jeremy P. Richards[a,c], Rui-Zhong Hu[a], Lei-Luo Xu[a], Jian-Feng Gao[a], Jing-Jing Zhu[a,c], Xing-Chun Zhang[a]

[a] State Key Laboratory of Ore Deposit Geochemistry, Institute of Geochemistry, Chinese Academy of Sciences, Guiyang 550081, PR China
[b] University of Chinese Academy of Sciences, Beijing 100049, PR China
[c] Mineral Exploration Research Centre, Harquail School of Earth Sciences, Laurentian University, 935 Ramsey Lake Road, Sudbury, Ontario P3E 2C6, Canada

ABSTRACT

The Yulong porphyry Cu-Mo ore district in eastern Tibet features a series of Eocene felsic porphyry intrusions, only one of which is intensively mineralized. In this study, zircon U-Pb ages, and major and trace element compositions of whole rock samples and in-situ accessory minerals (zircon, apatite and titanite) from these various intrusions were analyzed to determine the factors controlling Cu mineralization. New zircon U-Pb dating, together with published zircon U-Pb ages, suggest that these porphyry intrusions were emplaced over a relatively short period of time (43.9 ± 0.6 Ma to 40.9 ± 0.3 Ma), with the mineralized Yulong intrusion emplaced at a late stage of the magmatic activity (41.1 ± 0.3 Ma to 40.9 ± 0.3 Ma). These intrusions have indistinguishable whole-rock major and trace element compositions, but the mineralized Yulong intrusion has higher apatite and titanite La/Yb ratios (average apatite La/Yb = 115.1 ± 28.5, n = 52; average titanite La/Yb = 22.4 ± 4.9, n = 38) than the earlier subeconomic intrusions (average apatite La/Yb = 50.4 ± 12.3, n = 72; average titanite La/Yb = 12.4 ± 3.5, n = 58), suggesting more fractionation of amphibole from the magmas that sourced it. Additionally, a negative relationship between La/Yb and Ce_N/Ce_N^* ratios in apatite and titanite are interpreted to reflect increasing oxidation states through magma evolution.

Indistinguishable zircon Eu_N/Eu_N^* values and apatite core SO_3 contents from the mineralized (zircon $Eu_N/Eu_N^* = 0.69 \pm 0.06$, n = 25; apatite $SO_3 = 0.65 \pm 0.24$ wt%, n = 21) and subeconomic intrusions (zircon $Eu_N/Eu_N^* = 0.62 \pm 0.05$, n = 64; apatite $SO_3 = 0.61 \pm 0.27$ wt%, n = 15) suggest that the entire magmatic suite was relatively oxidized, hydrous and sulfur-rich, and was therefore fertile for ore-formation. However, apatite crystals from the mineralized Yulong intrusion have significantly lower Cl contents (0.08 ± 0.03 wt%, n = 72) and higher F/Cl ratios (47.80 ± 21.97, n = 72) than those from the subeconomic intrusions (Cl = 0.29 ± 0.29 wt%; F/Cl = 12.87 ± 5.16; n = 78). These data may reflect more extensive fluid exsolution from the parental magma chamber at the time of emplacement of the mineralizing Yulong magmas. Sudden and voluminous release of volatiles coeval with emplacement of the Yulong intrusion was triggered by an as yet unidentified process, but possibly including magmatic recharge.

1. Introduction

Magmatic oxidation and hydration states, sulfur contents and focused fluid exsolution processes are key factors controlling formation of porphyry Cu deposits (Burnham, 1979; Candela, 1992; Ballard et al., 2002; Richards, 2003, 2011a, 2015; Seedorff et al., 2005; Sillitoe, 2010). High magmatic oxidation state ($\Delta FMQ = +1$ to $+2$, where FMQ is the fayalite-magnetite-quartz buffer) means that most of the sulfur dissolved in the melt will be present as SO_4^{2-}, which prevents early Cu depletion by sulfide saturation or segregation (Metrich and Clocchiatti, 1996; Mungall, 2002; Richards, 2003, 2015; Jugo et al., 2005). High magmatic water content allow efficient and extensive exsolution of magmatic-hydrothermal fluids that are vital to the transportation and deposition of metals (Burnham, 1979; Candela, 1992; Richards, 2003, 2011b; Loucks, 2014).

At the deposit scale, porphyritic intrusions commonly occur in kilometer-scale clusters that were emplaced within several million years or less in time (e.g., the Yanacocha district, Peru, Longo et al.,

---

2010; the El Salvador district, Chile, Lee et al., 2017; the OK Tedi deposit, Papua New Guinea; Large et al., 2018). Porphyry Cu mineralization occurs in one or a few, but rarely all, of these intrusions, although they share many similarities (e.g., magmatic oxidation state). In this regard, revealing the factor(s) controlling ore formation within a porphyry ore deposit/district is of great significance to both mineral exploration and understanding the ore-forming processes.

Apatite, titanite and zircon are ubiquitous accessory minerals in granitic rocks (Frost et al., 2000; Bouzari et al., 2009; Belousova et al., 2002), which can accommodate abundant rare earth elements (REE) and trace elements in their crystal structures (Tiepolo et al., 2002; Webster and Piccoli, 2015; Lu et al., 2016). Additionally, apatite can incorporate halogens (e.g., F and Cl) and sulfur (Pan and Fleet, 2002). These minerals have chemical compositions that are sensitive to physico-chemical conditions in the crystallization environment, but relatively insensitive to later hydrothermal alteration and weathering (Tiepolo et al., 2002; Green and Pearson, 1986; Miles et al., 2014; Fu et al., 2016; Mao et al., 2016). Because of these characteristics, apatite, titanite and zircon have been widely used for studying the compositional and physico-chemical characteristics of parental magmas (Ding et al., 2015; Xu et al., 2015; Pan et al., 2016; Yang et al., 2018) and to track magmatic-hydrothermal processes (Boudreau and McCallum, 1989; Boyce and Hervig, 2009; Cao et al., 2015; Duan and Jiang, 2018).

The giant Yulong porphyry Cu-Mo deposit was emplaced in a postcollisional strike-slip fault system in eastern Tibet (Hou et al., 2003; Liang et al., 2006; Xu et al., 2012, 2016). It consists of one mineralized and several broadly coeval and co-magmatic subeconomic intrusions (Guo et al., 2006; Jiang et al., 2006; Tibet Yulong Copper Co., Ltd., 2009; Wang et al., 2009). Most of these subeconomic intrusions have not previously been dated, and the reason why they are only weakly mineralized remains unclear. In this study, we report new zircon U-Pb ages, whole-rock major and trace element compositions, and major and trace element composition of accessory minerals (zircon, apatite and titanite) for the Yulong intrusive suite, with the aim of clarifying the deposit-scale magmatic-hydrothermal processes that locally led to porphyry Cu mineralization. These data suggest that the entire Yulong intrusive suite was relatively oxidized, hydrous and sulfur-rich, and was therefore fertile for ore-formation. The late stage, ore-related Yulong intrusion was more extensively devolatilized, which was triggered by an as yet unidentified process, but possibly including magmatic recharge.

2. Geological background

2.1. The Yulong porphyry Cu belt

The collision between India and Asia at about 65–55 Ma (Yin and Harrison, 2000; Leech et al., 2005; Mo et al., 2007) gave rise to a series of large-scale strike-slip fault systems on the southeastern Tibetan plateau (Fig. 1; Zhang and Xie, 1997; Wang et al., 2001; Hou et al., 2003). The Jinshajiang-Red River strike-slip fault system, stretching from the Qiangtang terrane in the north to the Yangtze Craton in the south, is one of the largest of these systems. A number of Eocene alkaline porphyry intrusions and related porphyry Cu-Mo-Au deposits (e.g., the giant Beiya porphyry-skarn Au-Cu deposit, He et al., 2015; Deng et al., 2015; the Yao'an porphyry Au deposit, Bi et al., 2002, 2004, 2009; Bi et al., 1999, 2005) are distributed along this strike-slip fault system, forming the Jinshajiang-Red River alkali-rich igneous belt (Fig. 1; Zhang and Xie, 1997; Hu et al., 2004; Xu et al., 2012, 2016; Hu et al., 1998, 1999).

The Yulong porphyry Cu-Mo belt is situated in the Changdu-Simao block in the northern part of the JSRR belt (Figs. 1 and 2A), which consists of Proterozoic to early Paleozoic basement and middle Paleozoic–Mesozoic carbonate and clastic cover rocks (Tang and Luo, 1995; Hou et al., 2003). Over 20 porphyry Cu-Mo prospects have been discovered in the NW–SE-trending Yulong belt, at least seven of which

host significant Cu and Mo mineralization (Figs. 1 and 2A). These include the Yulong Cu-Mo deposit, the largest deposit among all the mineralized intrusions in the Yulong belt (1048 Mt at 0.62% Cu and 0.041% Mo; Tibet Yulong Copper Co., Ltd., 2009), the newly discovered Narigongma (144 Mt at 0.32% Cu; 43.6–41.7 Ma, Yang et al., 2014) and Baomai porphyry Cu deposits (96 Mt at 0.22% Cu; 42.7 Ma; Lin et al., 2018), and four previously documented porphyry Cu deposits (Zhanaga, 83 Mt at 0.36% Cu, 38.5 Ma; Mangzong, 74 Mt at 0.34% Cu, 37.5 Ma; Duoxiasongduo, 132 Mt at 0.38%, 37.2 Ma; Malasongduo, 227 Mt at 0.44% Cu, 37.1 Ma; Tang and Luo, 1995; Hou et al., 2003; Liang et al., 2006). The distribution of these deposits is suggested to be controlled by a series of NW–SE-trending, collision-related, secondary strike-slip faults (Hou et al., 2003; Xu et al., 2012; Yang et al., 2014; Lin et al., 2018).

2.2. Deposit geology

The Yulong Cu-Mo deposit is genetically related to, and mainly hosted by, the barrel-shaped Yulong intrusion, which intruded Triassic carbonate rocks and sandstones at the southern end of the SE-pitching Hengxingcuo anticline (Figs. 2B and 3). This anticline was formed prior to the emplacement of the Yulong intrusion, and was suggested to have provided a structural control on its emplacement (Tang and Luo, 1995; Tibet Yulong Copper Co., Ltd., 2009). Several ring-shaped, steeply-dipping faults were developed encircling the Yulong intrusion (Fig. 2B). They were formed by local compression due to the invasion of the Yulong intrusion (Tibet Yulong Copper Co., Ltd., 2009).

Multistage porphyry intrusions of the Yulong intrusion: The Yulong intrusion is a composite porphyry stock (Hou et al., 2003). However, the multistage porphyry intrusions are poorly revealed, and are inconsistent between different studies. For instance, Zhang et al. (1998) reported early stage quartz monzonite porphyry and late stage syenogranite porphyry, whereas an exploration report (Tibet Yulong Copper Co., Ltd., 2009) described three porphyry phases: monzongranite porphyry, granite porphyry and plagiogranite porphyry. However, no description or evidence for crosscutting relationships was provided in these studies. Most recently, based on detailed drill core logging and mutual crosscutting relationships, Chang et al. (2017) recognized three porphyry intrusions: early monzonitic granite porphyry (MGP), intermediate K-feldspar granite porphyry (KGP), and late quartz-albite porphyry (QAP; Fig. 3).

The MGP is a syn-mineralization porphyry and is characterized by abundant amphibole ($\sim$5 vol%), plagioclase (25–35 vol%), and K-feldspar (10–15 vol%) phenocrysts. The groundmass (40–50 vol%) is composed of fine-grained quartz, K-feldspar and plagioclase (Chang et al., 2017). The MGP accounts for the main volume of the Yulong intrusion (Fig. 3). Published zircon U-Pb isotope studies on the MGP yielded indistinguishable weighted mean zircon $^{206}Pb/^{238}U$ ages (2σ) of 40.9 $\pm$ 0.2 Ma to 41.3 $\pm$ 0.8 Ma (Guo et al., 2006; Liang et al., 2006; Wang et al., 2009; Li et al., 2012), except one slightly older age of 42.0 $\pm$ 0.3 Ma (Chang et al., 2017).

The KGP is also a syn-mineralization porphyry, but is much less voluminous compared to the MGP. It occurs as $<$ 50 m-wide dikes that intruded the MGP (Fig. 3), and contains phenocrysts of quartz (3–7 vol %), K-feldspar (10–25 vol%), and biotite (1–3 vol%) but very rare amphibole (Chang et al., 2017). The groundmass (70–80 vol%) is composed of fine-grained quartz and K-feldspar. The KGP has a zircon U-Pb age (2σ) of 41.2 $\pm$ 0.3 Ma (Chang et al., 2017).

The QAP is a late- to post-mineralization porphyry, and occurs as small dikes with thickness of $<$ 0.5–25 m (Fig. 3). Compared to the former two porphyries, the QAP has less abundant phenocrysts (15–20 vol%), which are mainly quartz (1 $\sim$ 2 vol%), plagioclase (10–15 vol%), and biotite (3–7 vol%), and very rare amphibole (Chang et al., 2017). The groundmass (80–85 vol%) is composed of quartz, K-feldspar, plagioclase and biotite. The QAP has been dated at 40.2 $\pm$ 0.3 Ma (2σ, zircon U-Pb; Chang et al., 2017), which is younger
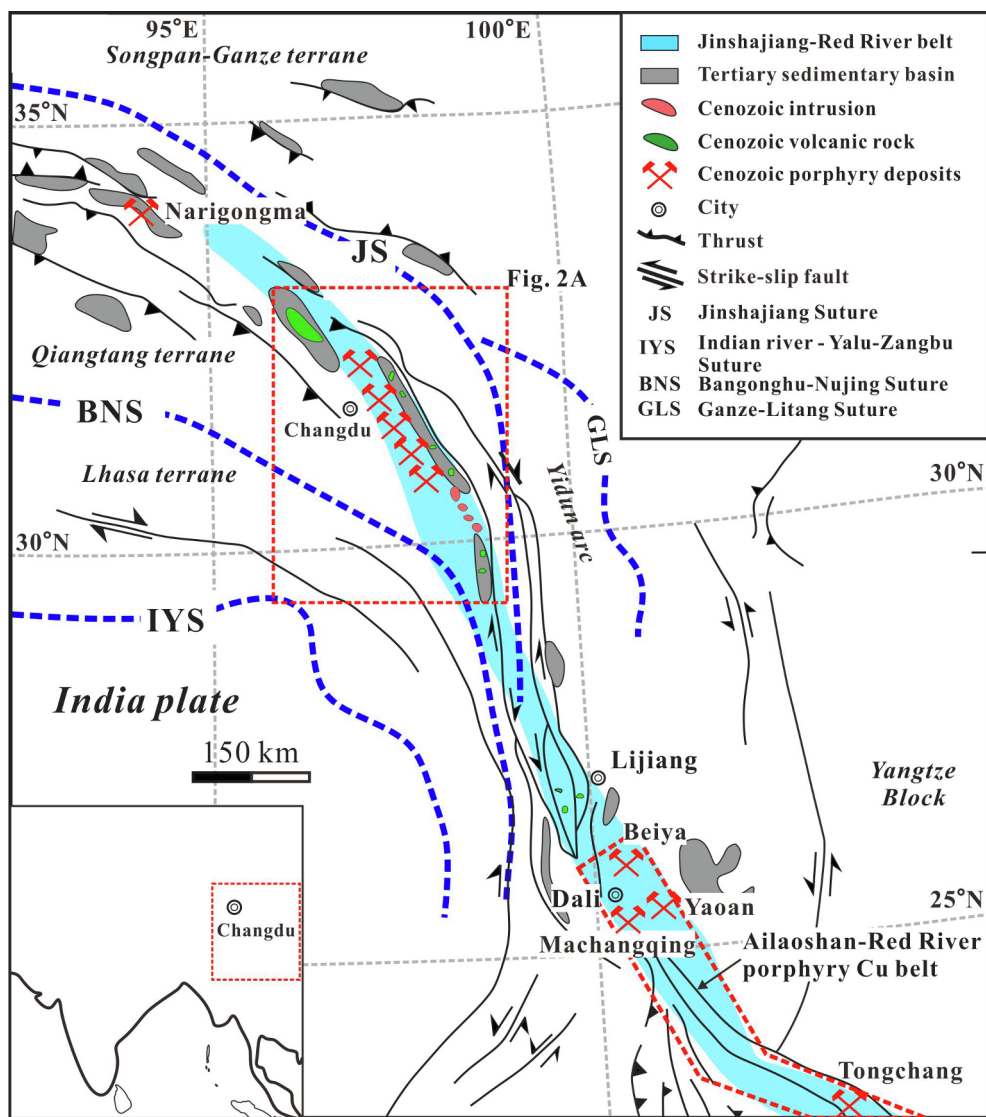
Fig. 1. A. Simplified geological map of the SE Tibet plateau, showing the location of representative porphyry deposits in the Cenozoic Jinshajiang-Red River porphyry Cu ± Mo ± Au deposit belt (Modified from Wang et al., 2001).

than the former two porphyries.

Hydrothermal alteration and mineralization: Based on the emplacement history of multistage porphyry intrusions, Chang et al. (2017) grouped the alteration and mineralization of the Yulong deposit into three stages: early, transitional, and late stages. The early stage alteration and mineralization occurred following the emplacement of the MGP, but predated the emplacement of the KGP dikes. It is characterized by potassic alteration associated with various types of veins, including biotite veins, barren quartz veins, granular quartz-dominated molybdenite + chalcopyrite veins, and chalcopyrite + molybdenite veins (Fig. 4A-C). The core of the Yulong intrusion has relatively low Cu and Mo grades, and is characterized by abundant barren quartz veins and biotite veins (Fig. 3; Chang et al., 2017). Other chalcopyrite- and molybdenite-bearing A veins are mainly localized in strong to weak potassic alteration zones adjacent to the barren core, as illustrated by the high Cu grade zones in Fig. 3. It is estimated that over 80% of the Cu and Mo at Yulong were deposited in this stage (Chang et al., 2017).

The transitional stage postdates the KGP dikes, but predates the QAP dikes (Chang et al., 2017). It is also characterized by strong to moderate potassic alteration and various types of A veins, which are similar to those in the early stages (Chang et al., 2017). Additionally, B-type veins also developed in this stage. The B veins generally contain

more abundant molybdenite than chalcopyrite (Fig. 4C-D). It is estimated that about ~20% of the Cu and Mo at Yulong were introduced in this stage (Chang et al., 2017).

The late stage alteration and mineralization postdate the emplacement of the QAP dikes (Chang et al., 2017). It is characterized by well-developed, feldspar-destructive sericitic alteration, as well as pyrite + quartz veins (Fig. 4E; D-type). The sericitic alteration commonly overprints the precursor potassic alteration. The D veins are distributed throughout the Yulong deposit. No economic Cu or Mo mineralization was produced in this stage (Chang et al., 2017).

Intensive argillic alteration developed in the upper part of the Yulong intrusion, and at the contacts between the intrusion and wall rocks (Fig. 3). It is expressed by the replacement of plagioclase phenocrysts by clay minerals such as kaolinite (Fig. 4D; Gu et al., 2003; Chang et al., 2017). This low temperature alteration overprints the previous potassic and sericitic alteration.

The timing of mineralization, constrained by ICP-MS molybdenite Re-Os dating, ranges from 41.3 ± 0.6 Ma to 39.7 ± 0.6 Ma (2σ, weighted mean = 40.6 ± 0.4 Ma, n = 9; Hou et al., 2006; Tang et al., 2009), which is indistinguishable from the zircon U-Pb ages of the Yulong intrusion. Based on detailed field relationships and extensive sampling of molybdenite-bearing veins, and high precision ID-NTIMS
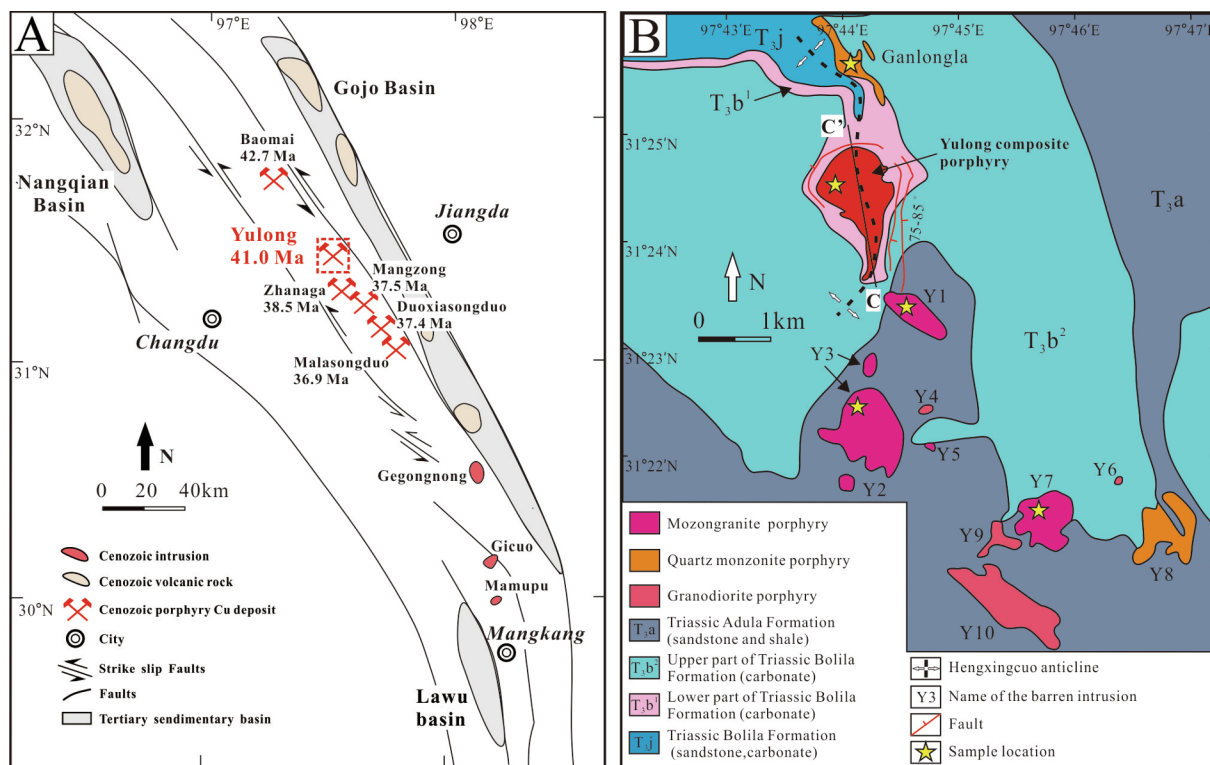
Fig. 2. A. Regional map of the Yulong porphyry Cu ± Mo deposit belt showing the distribution of porphyry Cu-Mo deposits (Modified from Hou et al., 2003; Lin et al., 2018). Location of the Yulong porphyry Cu-Mo deposit is shown in the box with red letters. B. Geological map of the Yulong ore district, showing the distribution of mineralized and subeconomic intrusions (Modified from unpublished report of the Tibet Yulong Copper Co., Ltd., 2009).
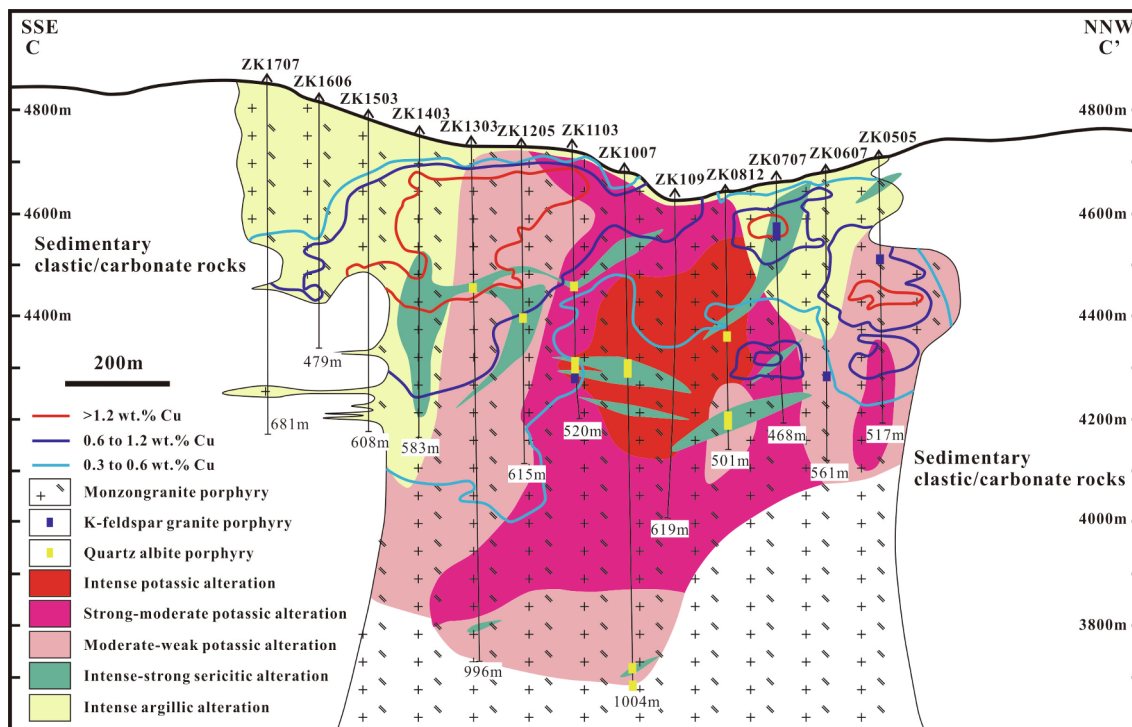

Fig. 3. Cross section C-C' through the mineralized Yulong intrusion, showing the distribution of multistage porphyry intrusions, hydrothermal alteration, and variation of Cu grades (Modified from Chang et al., 2017). See location of cross section C-C' in Fig. 2B.
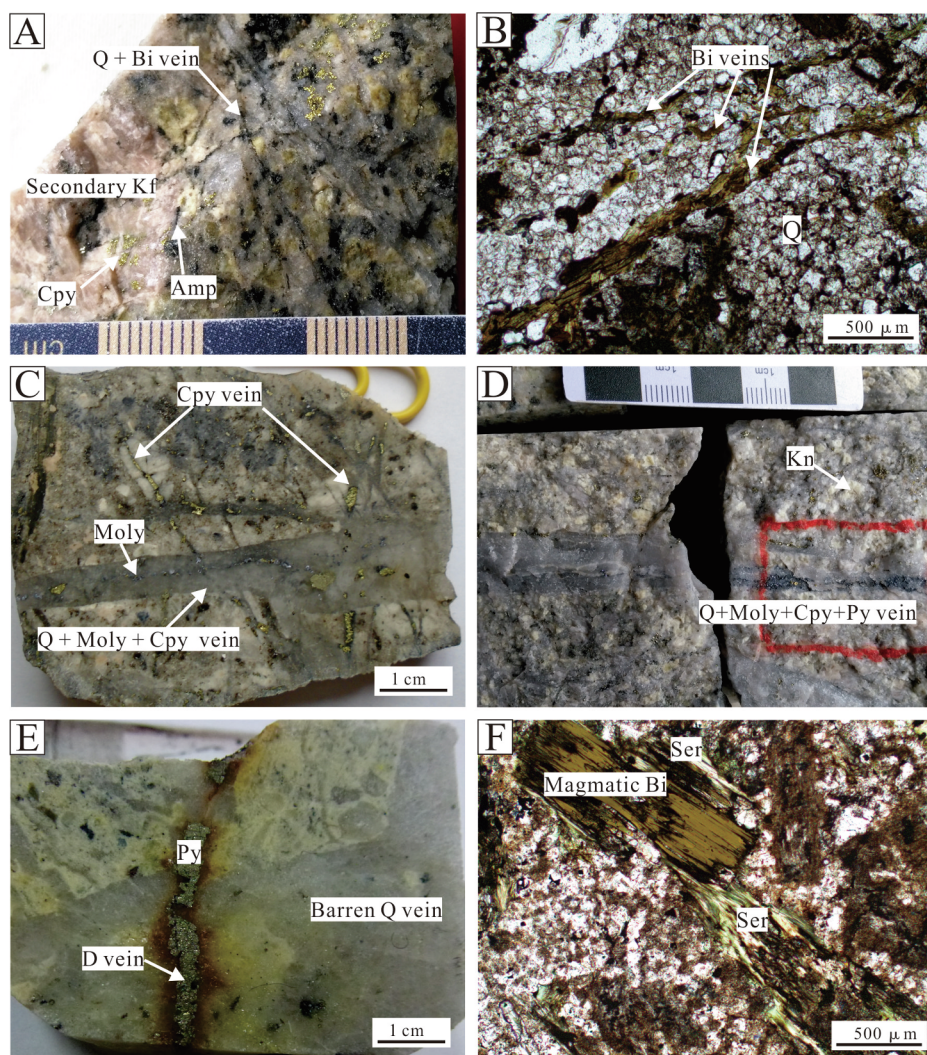
Fig. 4. Photographs showing the alteration and vein types within the MGP of the Yulong intrusion. A. Potassic alteration and disseminated chalcopyrite. Potassic alteration is expressed by the quartz + biotite A vein, and the secondary K-feldspar that enclose chalcopyrite (ZK0812-492m). B. Microphotograph of biotite A vein (ZK0806-180m). C. Quartz + molybdenite + chalcopyrite B vein (ZK0805-291m). The above B vein cut the previous chalcopyrite-dominated A veins. D. Quartz + molybdenite + chalcopyrite B vein (ZK1303-550m). The sample has experienced argillic alteration. E. Pyrite-quartz D vein in sample ZK0812-223m. This D vein cut the previous barren quartz A vein. F. Magmatic biotite altered to sericite, reflecting phyllic alteration (ZK1007-946m). Abbreviations: Amp = amphibole, Bi = biotite, Cpy = chalcopyrite, Kf = K-feldspar, Kn = kaolinite, Moly = molybdenite, Pl = plagioclase, Py = pyrite, Q = quartz, Ser = sericite.

molybdenite Re-Os dating, Chang et al. (2017) suggested that the Yulong deposit was produced over a period of ~5.1 m.y., but most of the Cu and Mo were deposited in a shorter duration of ~1.4 m.y. (Chang et al., 2017).

Subeconomic intrusions: Several subeconomic, weakly altered felsic intrusions were also emplaced in close spatial and temporal proximity to the mineralized Yulong intrusion (Fig. 2B; Tibet Yulong Copper Co., Ltd., 2009). They are mainly monzongranite porphyry, quartz monzonite porphyry, and granodiorite porphyry. Mineralogically they are composed of quartz, K-feldspar, plagioclase and biotite phenocrysts (Fig. 5A-B), similar to the MGP of the mineralized Yulong intrusion. Published studies reported weighted mean zircon ^{206}Pb/^{238}U ages (2σ) of 43.6 ± 0.8 Ma to 43.9 ± 0.6 Ma for the Ganlongla intrusion (Fig. 2B; Guo et al., 2006; Wang et al., 2009), and 41.4 ± 0.6 Ma for the Y3 intrusion (Wang et al., 2009). These ages are broadly within error of the ages of the mineralized Yulong intrusion. Jiang et al. (2006) and Wang et al. (2011) reported identical whole-rock Sr-Nd and zircon Hf isotopes of the mineralized MGP and subeconomic Ganlongla and Y3 intrusions, suggesting that they are probably co-magmatic. However, most of these subeconomic intrusions have not been dated, and the reason why these apparently comagmatic, closely emplaced intrusions are only weakly altered and mineralized remains unclear.

3. Sampling and analytical methods

Three drill core samples of MGP in the mineralized Yulong intrusion (ZK0812-389, ZK1007-607, and ZK1007-671) were collected for extraction of accessory minerals (zircon, apatite and titanite). The other eight samples of MGP were collected for whole-rock major and trace element analysis. The KGP and QAP proposed by Chang et al. (2017) were not recognized in the field, and therefore were not sampled in this study. For convenience of comparison with subeconomic intrusions, the MGP is referred to as the Yulong intrusion in the following text. Details of analytical methods for whole rock major and trace element analyses are provided in Appendix A. Samples of four subeconomic intrusions that are closest to the mineralized Yulong intrusion were collected from outcrops (sample YL1636 for the Y1 intrusion, YL1648 for the Y3, YL1647 for the Y7 intrusion, and YL1643 for the Ganlongla intrusion; Fig. 2B). Detailed sample locations, descriptions, and analyses applied to the collected samples are listed in Appendix Table A1.

3.1. CL/BSE imaging and EMPA analysis

Zircon, apatite and titanite were extracted from whole rock samples by using standard heavy liquid and magnetic techniques. The extracted
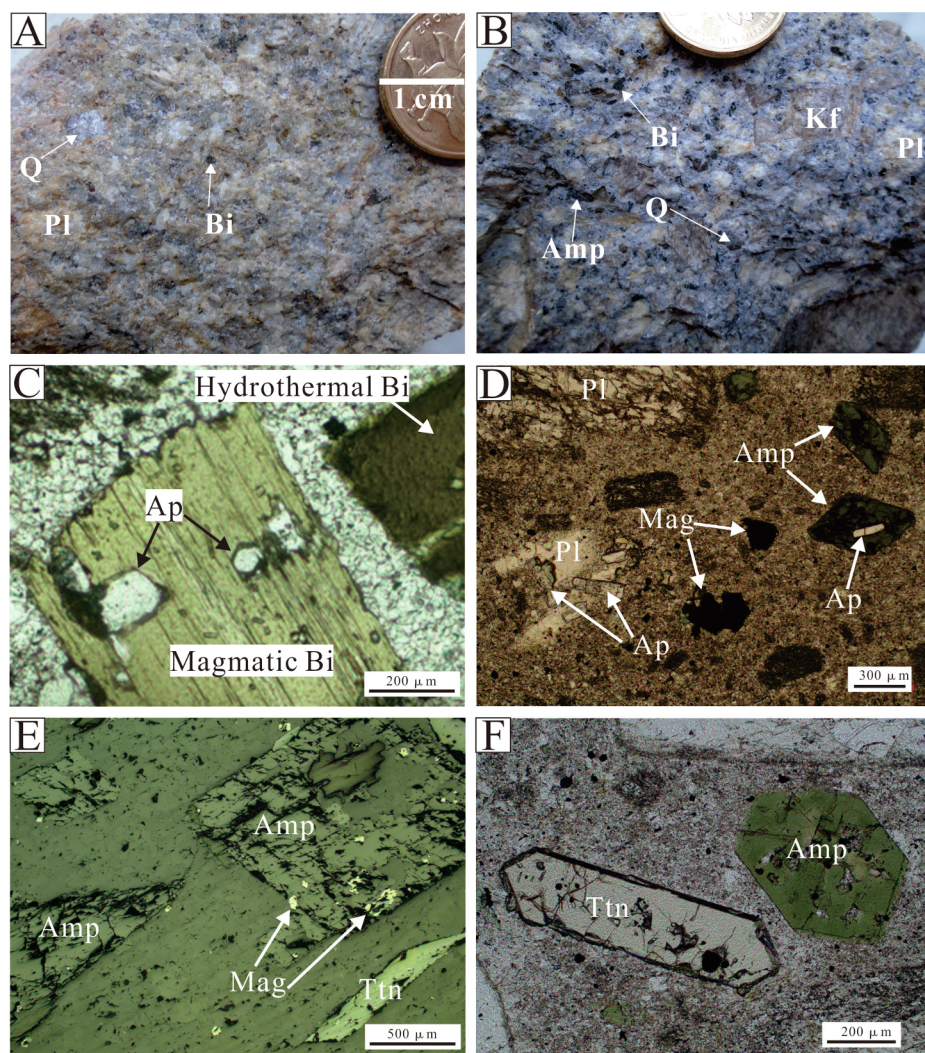
Fig. 5. A–B. Hand specimen photographs of the samples collected from the subeconomic Y3 and Y7 intrusions, respectively. They contain phenocrysts of quartz, K-feldspar, plagioclase, biotite and amphibole, which is similar to the MGP of the Yulong intrusion. C. Apatite crystals enclosed by magmatic biotite in the MGP of the Yulong intrusion (ZK1303-350m). D. Representative microphotographs showing apatite crystals enclosed by amphibole phenocrysts from the subeconomic intrusions (YL1647). E. Reflected light microphotographs showing titanite and amphibole phenocrysts in the MGP of the Yulong intrusion (ZK1007-454m). F. Representative microphotograph showing titanite and amphibole phenocrysts from the subeconomic intrusions (YL1643). Abbreviations: Amp = amphibole, Ap = apatite, Bi = biotite, Kf = K-feldspar, Mag = magnetite, Pl = plagioclase, Q = quartz, Ttn = titanite.

mineral grains were mounted in epoxy and then polished to about half-grain thickness. Transmitted and reflected light photographs of these minerals were taken to reveal other mineral inclusions, which were avoided during electron microprobe analysis (EMPA) and laser-ablation inductively-coupled-plasma mass spectrometry (LA-ICP-MS) analysis. Cathodoluminescence (CL, zircon and apatite) and back-scattered electron imaging techniques (BSE, titanite) were further applied to help select suitable spots for EMPA and LA-ICP-MS analysis. Detailed analytical methods are described in Appendix A.

3.2. Zircon U-Pb dating

Zircon secondary ion mass spectrometry (SIMS) U-Pb dating of samples ZK0812-389, ZK1007-607 and YL1636 was performed at the Guangzhou Institute of Geochemistry, Chinese Academy of Sciences. Zircon LA-ICP-MS U-Pb dating of samples YL1643, YL1647, and YL1648 was conducted at the State Key Laboratory of Ore deposit Geochemistry (SKLODG), Institute of Geochemistry, Chinese Academy of Sciences (IGCAS). Detailed analytical methods are described in Appendix A.

3.3. Laser-ablation ICP-MS trace element analysis of zircon, titanite and apatite

In-situ LA-ICP-MS trace element analysis of zircon, titanite, and apatite were conducted at SKLODG, IGCAS. For apatite and titanite, every analytical spot was analyzed by EMPA in advance. For zircons

that were dated by LA-ICP-MS, trace element compositions were obtained simultaneously with U-Pb isotopic compositions. For zircons that were dated by SIMS, the trace element compositions were obtained by LA-ICP-MS analysis on the spots that were previously used for SIMS dating. Detailed analytical methods are described in Appendix A.

4. Results

4.1. Zircon U-Pb ages

Zircons extracted from selected samples are generally colorless and euhedral in shape. CL images reveal that they mostly show good oscillatory zoning, indicating a magmatic origin (Fig. 6A; Corfu et al., 2003). Zircons with obvious inherited cores or inclusions under CL images were avoided during SIMS and LA-ICP-MS analysis. Zircon U-Pb results of LA-ICP-MS and SIMS are listed in Appendix Tables A2 and A3, respectively.

MGP of the Yulong intrusion: Two samples (sample ZK0812-389 and sample ZK1007-607) were dated in this study. Twenty one analyses were carried out on sample ZK0812-389. Of these, two analyses (ZK0812-389#05, #11) are interpreted to be of inherited zircons with apparent ages of 46.4 ± 0.7 Ma and 1166 ± 23.3 Ma. The remaining 19 analyses are concordant and yield a weighted mean $^{206}Pb/^{238}U$ age of 41.0 ± 0.3 Ma (2σ, MSWD = 1.2). Nevertheless, two of the remaining 19 analyses (ZK0812-389#04, #14) have slightly older $^{206}Pb/^{238}U$ ages (42.0 Ma and 42.3 Ma), which are interpreted as
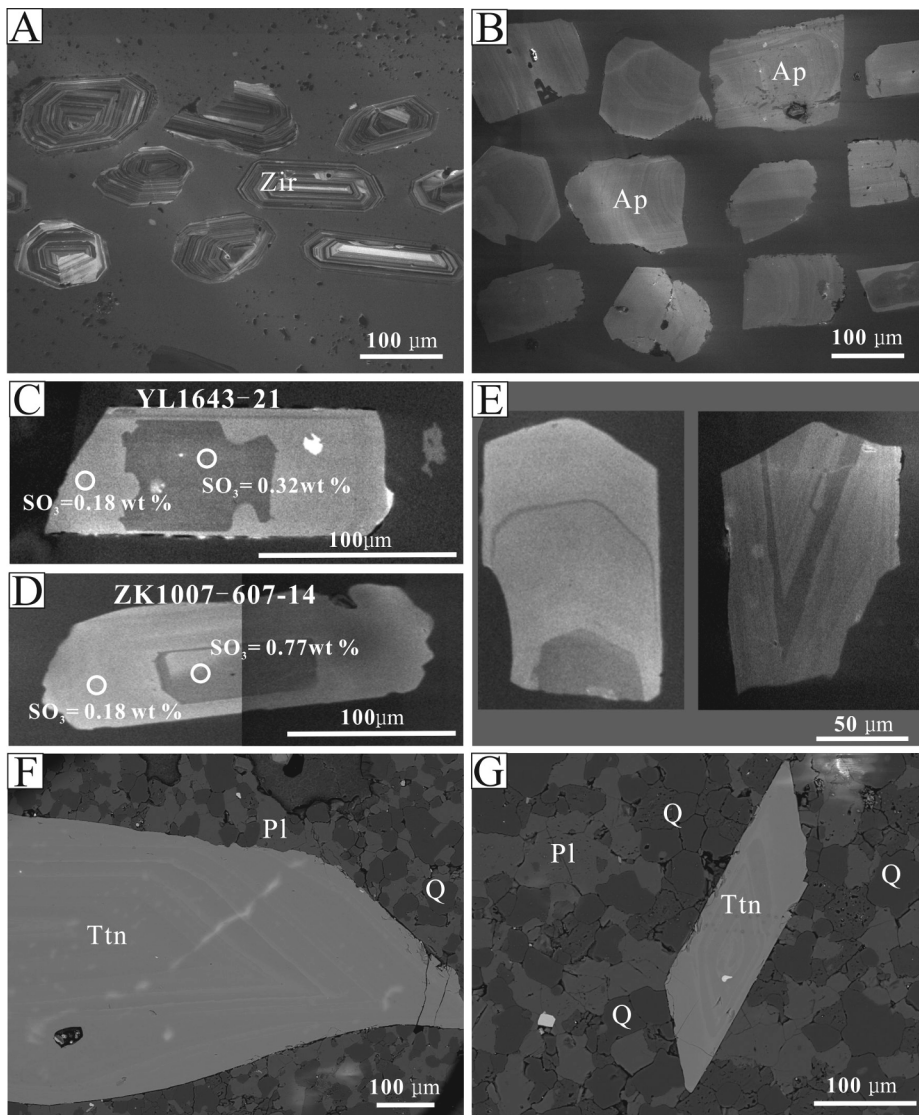
Fig. 6. A. Cathodoluminescence (CL) image of zircons extracted from the MGP of the mineralized Yulong intrusion, showing good oscillatory zonings and indicating magmatic origin (ZK1007-607m). B. Representative image showing oscillatory zoning of apatite crystals from subeconomic intrusions (YL1636). C–D. CL images show zoning from SO_3-rich core (CL-dark) to SO_3-poor rim (CL-bright) in some apatite crystals from the mineralized (ZK1007-607m) and subeconomic intrusions (YL1643). E. CL images showing cyclical zonation of CL-dark and CL-bright zones of apatite crystals from the mineralized Yulong intrusion (ZK1007-607m). F–G. Back-scattered secondary electron images showing oscillatory zoning in titanite crystals from MGP of the Yulong intrusion (sample YL1523; see location in Appendix Table A1). Abbreviations: Ap = apatite, Pl = plagioclase, Q = quartz, Ttn = titanite, Zir = zircon.

antecrysts, and four analyses (ZK0812-389#06, #07, #12 and #15) have slightly younger $^{206}Pb/^{238}U$ ages, possibly reflecting Pb loss. If these six analyses are excluded, the remaining 13 analyses yield a weighted mean $^{206}Pb/^{238}U$ age of 41.1 ± 0.3 Ma (2σ, MSWD = 0.3; Fig. 7A), which is almost identical to the age calculated from 19 analyses, but with a slightly improved MSWD. We therefore consider this result to be best age estimate of sample ZK0812-389.

Twenty zircon crystals were analyzed from sample ZK1007-607. One analysis (ZK1007-607#07) has an older $^{206}Pb/^{238}U$ age of 64.2 ± 6.5 Ma, and is interpreted to be an inherited zircon. Two other analyses (ZK1007-607#02 and #04) have slightly older ages (42.4 ± 0.6 Ma and 42.3 ± 0.6 Ma) than the main population, and are interpreted to be antecrysts, whereas one analysis (ZK1007-607#15) has a slightly younger $^{206}Pb/^{238}U$ age (39.5 ± 0.6 Ma), possibly due to Pb loss. The remaining 16 analyses are concordant and yield a weighted mean $^{206}Pb/^{238}U$ age of 40.9 ± 0.3 Ma (2σ, MSWD = 0.4; Fig. 7B). This age is considered to be the best estimate of the age of sample ZK1007-607.

Y1 intrusion (sample YL1636): Twenty two zircon crystals were analyzed from the Y1 intrusion. One of these analyses (YL1636#14) is of inherited zircon with an age of 942 ± 13.2 Ma. Two other analyses (YL1636#15 and #22) were excluded from the age calculation due to their large error in measured $^{207}Pb/^{235}U$, probably due to high contents of common Pb. The remaining 19 analysis are concordant and yielded a weighted mean $^{206}Pb/^{238}U$ age of 41.7 ± 0.3 Ma (2σ, MSWD = 1.0; Fig. 7C).

Ganlongla intrusion (sample YL1643): Nineteen zircon crystals were analyzed from the Ganlongla intrusion, 17 of which are concordant and yield a weighted mean $^{206}Pb/^{238}U$ age of 41.8 ± 0.3 Ma (2σ, MSWD = 0.6; Fig. 7D). The other two analyzed zircons (YL1643#2 and #16) are inherited, with $^{206}Pb/^{238}U$ age ages of 258 ± 3.2 Ma and 128 ± 2.0 Ma, respectively.

Y7 intrusion (sample YL1647): Twenty five zircon crystals were analyzed from the Y7 intrusion, 21 of which yielded a weighted mean $^{206}Pb/^{238}U$ age of 41.8 ± 0.2 Ma (2σ, MSWD = 0.6; Fig. 7E). The remaining four analyses (YL1647#2, #6, #17 and #23) are of inherited zircons with $^{206}Pb/^{238}U$ ages ranging from 247 to 1048 Ma.

Y3 intrusion (sample YL1648): Twenty two zircon crystals were analyzed from the Y3 intrusion, all of which were concordant and yielded a weighted mean $^{206}Pb/^{238}U$ age of 42.3 ± 0.2 Ma (2σ, MSWD = 0.7; Fig. 7F).

4.2. Whole rock geochemistry

New major and trace element geochemical data of the mineralized and subeconomic intrusions are combined with analyses from Jiang et al. (2006); all data are listed in Appendix Table A4 and plotted in Fig. 8. The mineralized and subeconomic intrusions are felsic, and have

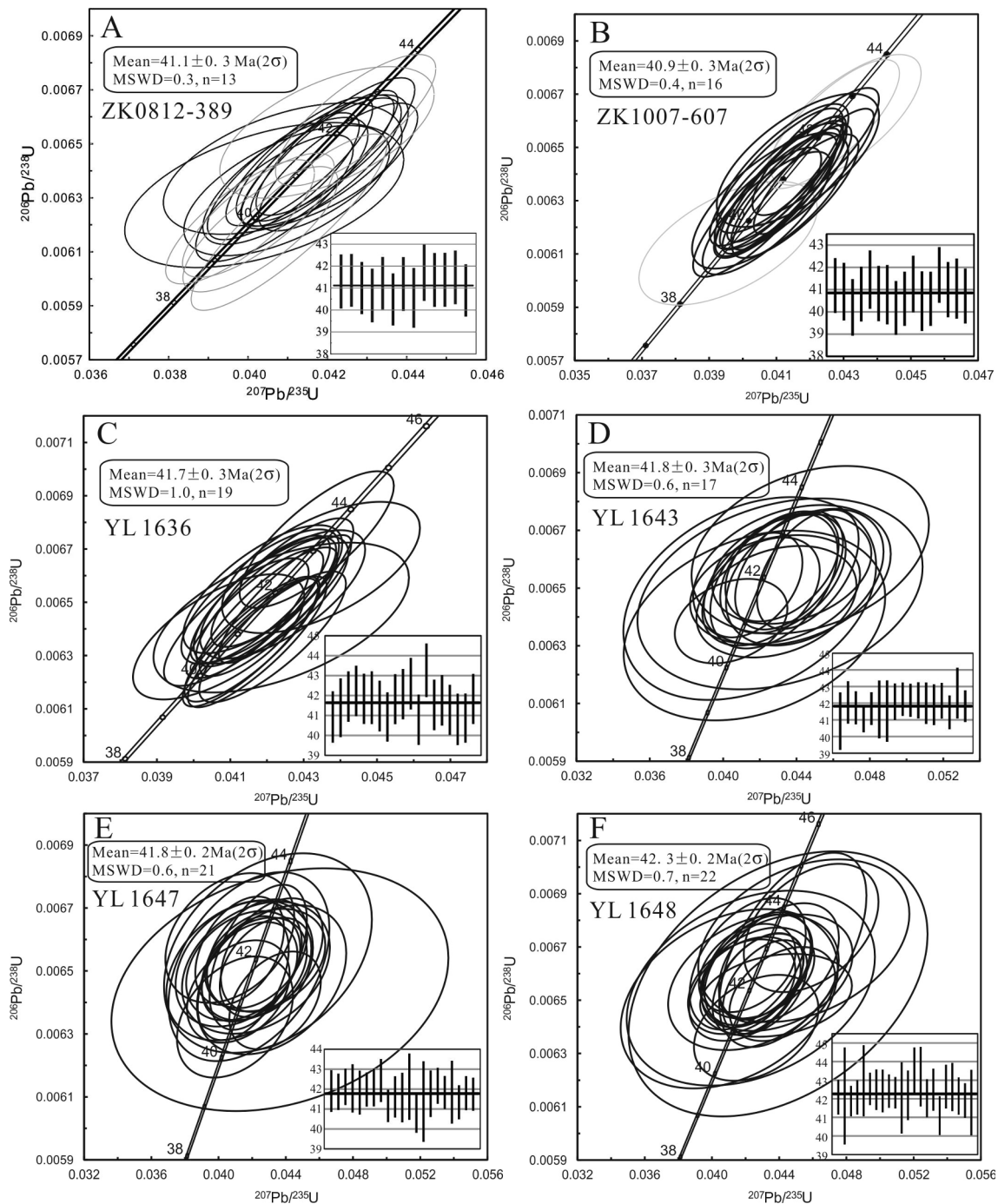**Fig. 7.** Zircon U-Pb Concordia plots with inserted weighted mean $^{206}Pb/^{238}U$ ages for the samples from mineralized and subeconomic intrusions in the Yulong ore district.

broadly indistinguishable major element compositions (e.g., $SiO_2 = 67.8$–74.8 wt%) with moderate to high loss-on-ignition values (LOI: 0.8–3.3%, with the exception of 6.1% for sample YL911; Appendix Table A4), reflecting varying degrees of potassic and sericitic alteration. In a Zr/Ti versus Nb/Y diagram, samples from this study mainly plot in the syenite field, whereas samples from Jiang et al. (2006) mainly plot close by but in the granite field (Fig. 8A). In addition, while the data from Jiang et al. (2006) show higher La/Yb ratios for the mineralized Yulong intrusion, this is not observed in our data (Fig. 8B). We are unable explain these discrepancies but, nonetheless, in chondrite-normalized rare earth element (REE) diagrams, all these samples have right inclined, listric-shaped patterns (Fig. 8C), suggesting

fractionation of amphibole during magma evolution (Romick et al., 1992; Castillo et al., 1999; Rooney et al., 2011; Richards, 2011b).

4.3. Compositions of zircon, apatite and titanite

Laser ablation-ICP-MS trace element analyses of zircon from these intrusions are illustrated in Figs. 9 and 10, and listed Appendix Table A5. The EMPA major and LA-ICP-MS trace element compositions of apatite are listed in Appendix Tables A6 and A7, respectively, and illustrated in Figs. 9 and 11. The EMPA major and LA-ICP-MS trace element compositions of titanite are listed in Appendix Tables A8 and A9, respectively, and illustrated in Figs. 9 and 12. LA-ICP-MS trace
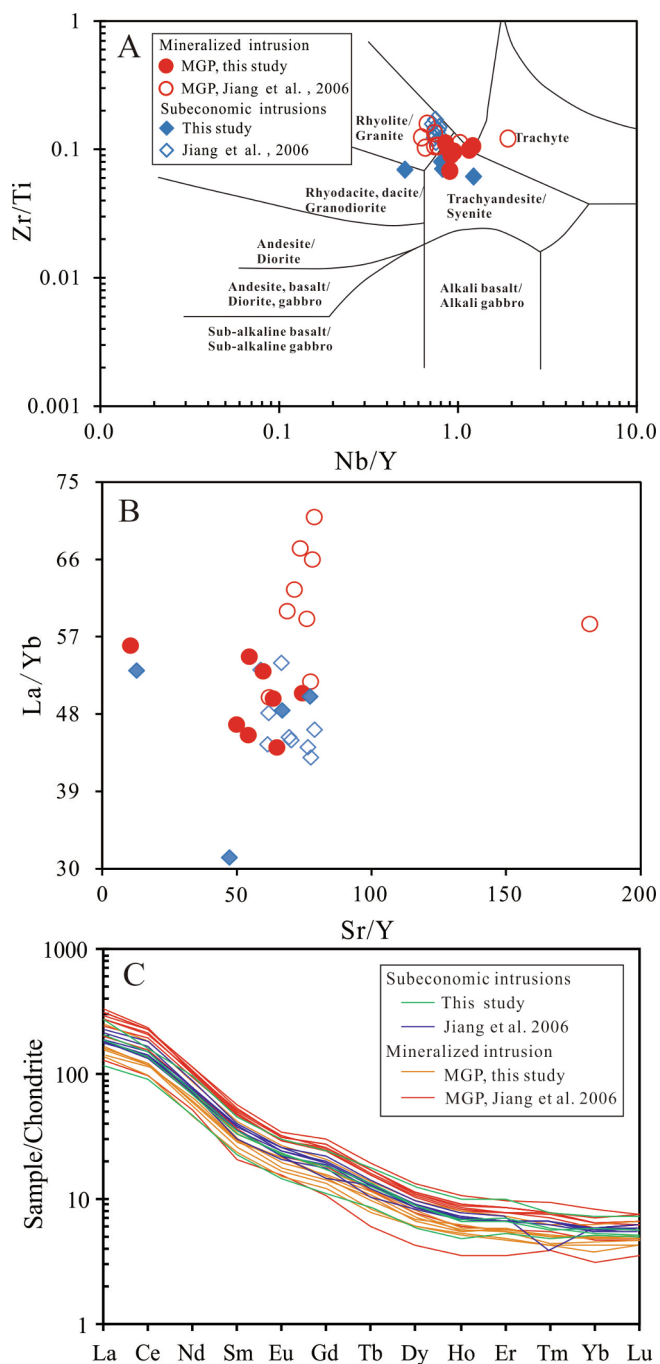
Fig. 8. Whole-rock geochemical features of the mineralized and subeconomic intrusions in the Yulong ore district. A. Zr/Ti vs. Nb/Y discrimination diagram (Winchester and Floyd, 1977). B. La/Yb vs. Sr/Y diagram. C. Chondrite-normalized whole-rock REE patterns. Chondrite normalization values are from Sun and McDonough (1989).

Fig. 9. Chondrite-normalized REE diagrams of (A) zircon, (B) apatite and (C) titanite from mineralized and subeconomic intrusions in the Yulong ore district. Chondrite normalization values are from Sun and McDonough (1989).

element compositions of standards NIST610 and NIST612 used for zircon, apatite and titanite analysis are listed in Appendix Table A10.

Zircon: During zircon LA-ICP-MS analyses, it is common to encounter small mineral inclusions such as apatite and titanite (Lu et al., 2016). In this study, La > 1 ppm was taken as criteria to reflect apatite contamination (Lu et al., 2016), and such data were excluded. Low Ti (< 20 ppm) and Ta (< 2 ppm) contents in all analyses suggest no contamination from titanites. Chondrite-normalized REE patterns of zircon crystals from both mineralized and subeconomic intrusions are similar, and are characterized by positive Ce anomalies, small negative Eu anomalies, and depletion of light rare earth elements (LREE) relative
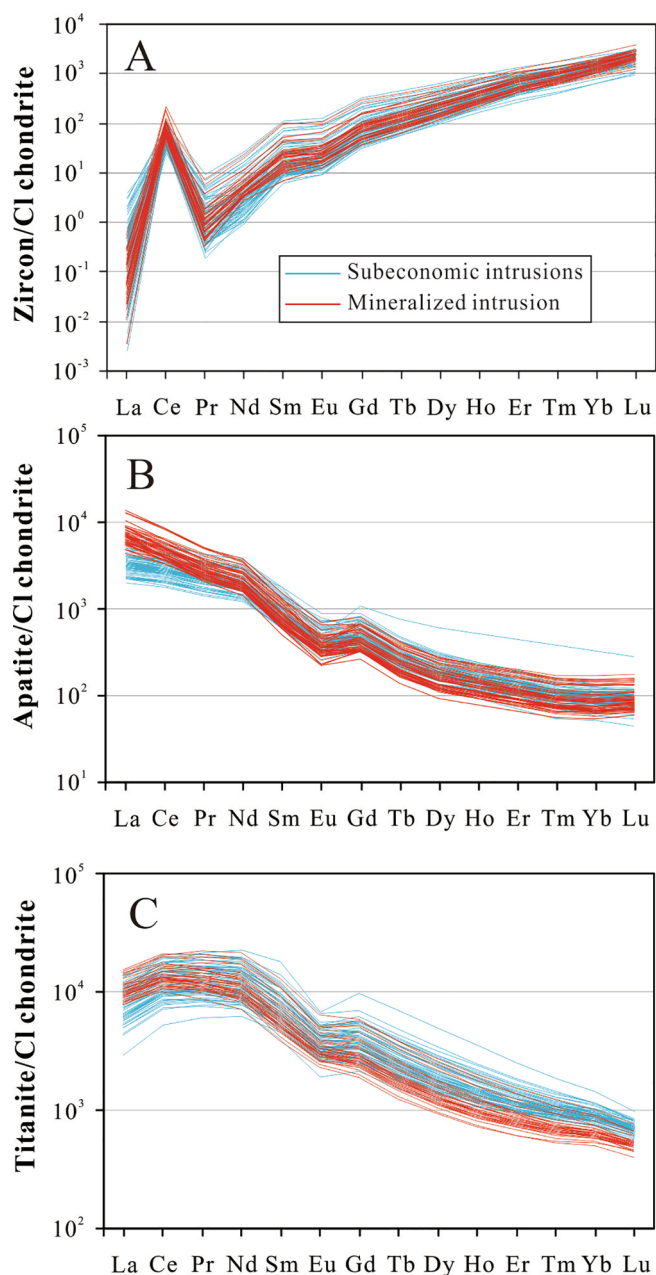
to heavy rare earth elements (Fig. 9A).

Zircon trace element ratios such as Eu_N/Eu_N^* ($Eu_N/Eu_N^* = Eu_N/(Sm_N \times Gd_N)^{0.5}$) and $10,000*(Eu_N/Eu_N^*)/Y$ were proposed to be proxies of oxidation and hydration states of the parent magma (e.g., Ballard et al., 2002; Dilles et al., 2015; Lu et al., 2016). Recently, Loader et al. (2017) have shown that zircon Eu_N/Eu_N^* values could also be strongly affected by the co-crystallization of titanite. However, no titanite mineral inclusions were observed in zircons from this study (Fig. 6A). In addition, all the analyzed zircons have Ta contents ranging from 0.24 ppm to 1.87 ppm (Appendix Table 5), which are distinct from zircons co-crystallized with titanite (< 0.2 ppm; Loader et al., 2017), but similar to zircons that are not affected by titanite co-crystallization (0.2–2 ppm; Loader et al., 2017). This suggests that zircon crystallization preceded titanite crystallization at Yulong. We therefore conclude that the zircon Eu anomalies in this study could be used to qualitatively estimate the redox condition of parent magmas. The Eu_N/Eu_N^*
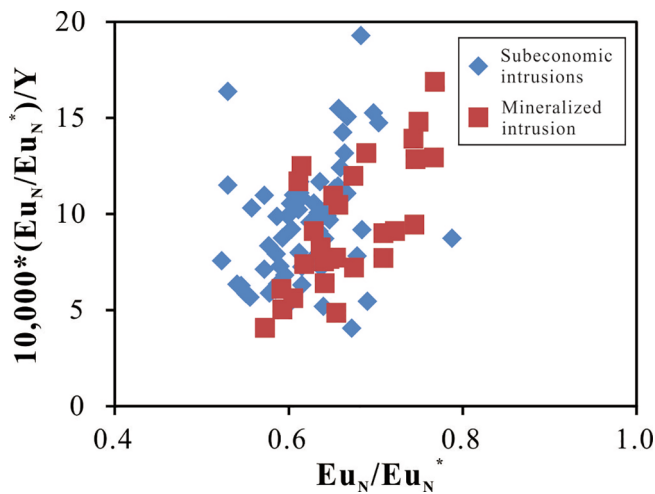
Fig. 10. Zircon $10,000*(Eu_N/Eu_N^*)/Y$ vs. Eu_N/Eu_N^* diagram. Eu_N/Eu_N^* is the europium anomaly which was calculated as $Eu_N/\sqrt{Sm_N*Gd_N}$, where N indicates the chondrite-normalized value. Chondrite normalization values are from Sun and McDonough (1989).

and $10,000*(Eu_N/Eu_N^*)/Y$ values mostly overlap between mineralized ($Eu_N/Eu_N^* = 0.59$–0.77, average $= 0.69 \pm 0.06$; $10,000*(Eu_N/Eu_N^*)/Y = 4.08$–$16.86$, average $= 9.44 \pm 3.30$; n = 27) and subeconomic intrusions ($Eu_N/Eu_N^* = 0.52$–0.79, average $= 0.62 \pm 0.05$; $10,000*(Eu_N/Eu_N^*)/Y = 4.05$–$19.27$, average $= 9.47 \pm 3.07$; n = 64), suggesting similar and relatively high oxidation states and water contents of these intrusions (Fig. 10).

Apatite: Apatite grains from all selected samples are colorless and generally rectangular in shape, with length:width ratios ranging from 1:1 to 3:1 (Figs. 5C-D and 6B-E). Many apatite crystals occur as inclusions in phenocrysts such as biotite and amphibole (Fig. 5C-D). The apatite crystals show oscillatory zoning in CL images (Fig. 6B-E). In addition, they have right-inclined chondrite-normalized REE patterns (Fig. 9B) that differ significantly from hydrothermal apatite (e.g., Chen et al., 2019), suggesting a magmatic origin. A few apatite grains, from both the mineralized and subeconomic intrusions, have CL-dark cores that abruptly zone to CL-bright rims (Fig. 6C-D). These apatite cores have higher SO_3 contents (mineralized intrusion: $SO_3 = 0.11$–0.95 wt%, average $= 0.65 \pm 0.24$ wt%, n = 21; subeconomic intrusions: $SO_3 = 0.29$–1.14 wt%, average $= 0.61 \pm 0.27$ wt%, n = 15) than the rims and normal apatites (where no core-rim textures were observed) (mineralized intrusion: $SO_3 = 0.07$–0.55 wt%, average $= 0.21 \pm 0.10$ wt%, n = 47; subeconomic intrusions: $SO_3 = 0.01$–0.47 wt%, average $= 0.15 \pm 0.07$ wt%, n = 63; Table A6; Figs. 6C–D, and 11B). Similar apatite core-rim textures have been previously reported at other porphyry Cu deposits (e.g., the Yerington batholith, Streck and Dilles, 1998; the Galore Creek porphyry Cu-Mo deposit, Liaghat and Tosdal, 2008), and were argued to reflect SO_2 degassing or anhydrite crystallization from a relatively oxidized, sulfur-rich magma (Streck and Dilles, 1998). Therefore, the apatite core-rim textures at Yulong are interpreted to reflect high initial sulfur contents and oxidation states of the magma. Additionally, some apatite grains from the mineralized Yulong intrusion are characterized by abrupt and cyclical zonation of CL-dark and CL-bright zones (Fig. 6E). This suggests that these apatite grains crystallized from a periodically evolving magma (e.g., Cao et al., 2014).

All the analyzed apatite crystals are characterized by enrichments of

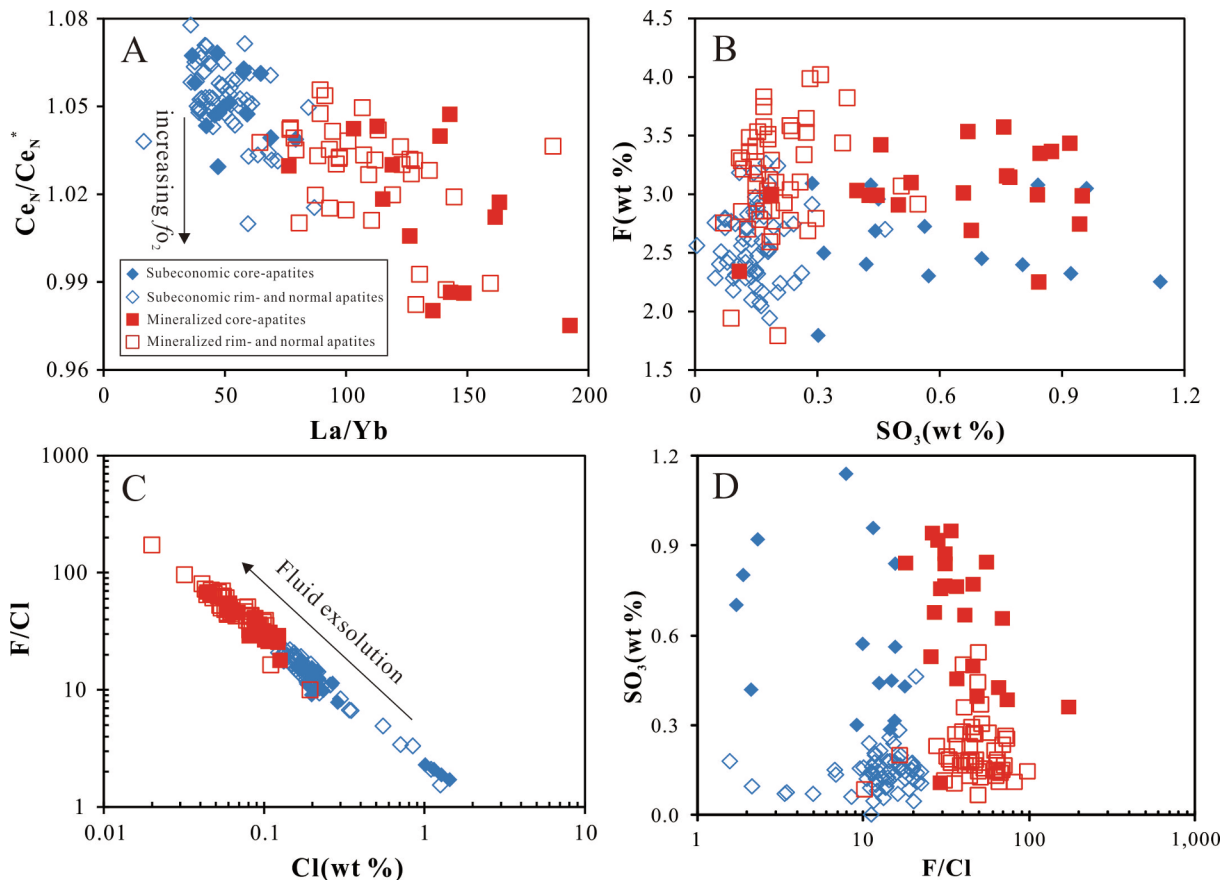**Fig. 11.** Trace element and halogen and sulfur compositions for apatite crystals from the mineralized and subeconomic intrusions. A. Ce_N/Ce_N^* vs. La/Yb. B. SO_3 vs. F. C. F/Cl vs. Cl. D. F/Cl vs. SO_3. Ce_N/Ce_N^* is the cerium anomaly which was calculated as $Ce_N/\sqrt{La_N*Pr_N}$, where N indicates the chondrite-normalized value. Chondrite normalization values are from Sun and McDonough (1989).
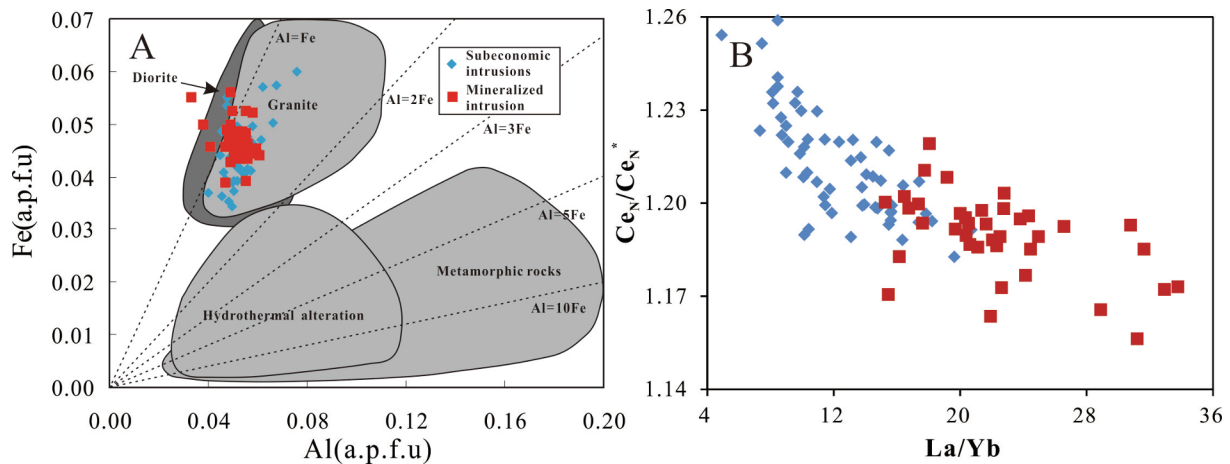
Fig. 12. Major and trace element compositions for titanite crystals from the mineralized and subeconomic intrusions. A. Al (a.p.f.u) vs. Fe (a.p.f.u), showing that the titanites in this study are of magmatic origin (after Aleinikoff et al., 2002; the field of hydrothermal titanite is from Cao et al., 2015). B. Ce_N/Ce_N^* vs. La/Yb. Ce_N/Ce_N^* is the cerium anomaly which was calculated as $Ce_N/sqrt(La_N*Pr_N)$, where N indicates the chondrite-normalized value. Chondrite normalization values are from Sun and McDonough (1989).

LREE relative to HREE on chondrite-normalized diagrams (Fig. 9B). Those from the mineralized Yulong intrusion have higher La/Yb (64.5–192.4, average = 115.1 ± 28.5, n = 52) and slightly lower Ce_N/Ce_N^* ratios (0.98–1.06, average = 1.02 ± 0.02, n = 52; $Ce_N/Ce_N^* = Ce_N/(La_N × Pr_N)^{0.5}$) than those of the subeconomic intrusions (La/Yb = 16.6–87.0, average = 50.4 ± 12.3; Ce_N/Ce_N^* = 1.01–1.08, average = 1.05 ± 0.01; n = 72; Fig. 11A; Appendix Table 7). Although the average apatite Ce_N/Ce_N^* values of the mineralized and subeconomic intrusions are similar, a statistical test (*t*-test) of these two groups of data yields p-value of $8.7 × 10^{-16}$, which is significantly lower than 0.05. This indicates that these two groups of data are statistically different. A negative correlation between apatite La/Yb and Ce_N/Ce_N^* ratios was found (Fig. 11A). Additionally, apatite crystals from the mineralized Yulong intrusion have lower Cl contents (0.02–0.19 wt%, average = 0.08 ± 0.03 wt%, n = 68), higher F contents (1.79–4.02 wt%, average = 3.13 ± 0.43 wt%, n = 68), and therefore higher F/Cl ratios (10.0–171.8, average = 47.7 ± 22.2, n = 68) than those from the subeconomic intrusions (Cl = 0.12–1.44 wt%, average = 0.29 ± 0.29 wt%; F = 1.80–3.26 wt %, average = 2.57 ± 0.33 wt%; F/Cl = 1.54–21.94, average = 12.87 ± 5.16; n = 78; Fig. 11B-D).

Titanite: Titanite crystals from both mineralized and subeconomic intrusions show similar petrographic characteristics under transmitted and reflect light: colorless or light brown, 200–1,000 μm in size, and euhedral to sub euhedral in shape (Fig. 5E-F). They show oscillatory zoning in BSE images (Fig. 6F-G), which suggests that they are of magmatic origin and not altered by hydrothermal fluids (Aleinikoff et al., 2002). This is also evidenced by the relatively low Al (0.03–0.08 a.p.f.u.), high Fe (0.03–0.10 a.p.f.u.), and low Al (a.p.f.u)/Fe (a.p.f.u) ratios (0.54–1.45, average = 1.16 ± 0.16, n = 96) of the analyzed titanite crystals, which are characteristic of magmatic titanite in diorite and granite (Fig. 12A; Aleinikoff et al., 2002; Cao et al., 2015).

All analyzed titanite crystals show enrichments of LREE relative to HREE on chondrite-normalized REE diagrams, with maximum values for Ce-Pr-Nd, and lower values for La and heavier REE (typical patterns for titanite; Fig. 9C). Titanites from the mineralized Yulong intrusion have higher La/Yb (15.3–33.8, average = 22.4 ± 4.9, n = 38) and slightly lower Ce_N/Ce_N^* ratios (1.16–1.22, average = 1.19 ± 0.01, n = 38) than those of the subeconomic intrusions (La/Yb = 4.9–20.7, average = 12.4 ± 3.5; Ce_N/Ce_N^* = 1.18–1.26, average = 1.21 ± 0.02; n = 38; n = 58; Fig. 12B). A statistical test (*t*-test) of the titanite Ce_N/Ce_N^* values of the mineralized and subeconomic intrusions yields p-value of $7.8 × 10^{-10}$, which is significantly lower than 0.05. This indicates that these two groups of data are statistically different. Similar

to the apatite, we found a negative relationship between titanite La/Yb and Ce_N/Ce_N^* ratios (Fig. 12B).

5. Discussion

5.1. Temporal relationship between mineralized and subeconomic intrusions

The subeconomic intrusions in the Yulong ore district were emplaced at ~42 Ma (Y3 intrusion, 42.3 ± 0.2 Ma; Y7 intrusion, 41.8 ± 0.2 Ma; Ganlongla intrusion, 41.8 ± 0.3 Ma; Y1 intrusion, 41.7 ± 0.3 Ma; Fig. 7C-F), whereas the mineralized Yulong intrusion has slightly younger zircon U-Pb ages of 41.1 ± 0.3 Ma and 40.9 ± 0.3 Ma, respectively (Fig. 7A-B). In addition, several zircon grains from the mineralized intrusion are likely to be antecrysts, with older ages of 42.4–42.0 Ma that are very similar to the ages of the subeconomic intrusions (Fig. 7A-B). These zircon antecrysts also have similar zircon trace element compositions with those of the mineralized and subeconomic intrusions (Appendix Table 5). Thus we conclude that the mineralized Yulong intrusion was up to ~1 m.y. younger than, but broadly comagmatic, with the subeconomic intrusions.

5.2. Oxidation/hydration states and sulfur contents of the intrusions

Higher zircon Eu_N/Eu_N^* and $10,000*(Eu_N/Eu_N^*)/Y$ values are generally interpreted to suggest higher oxidation and hydration states of the parent magma due to the preferred incorporation of Eu^{3+} into zircons (Ballard et al., 2002; Dilles et al., 2015; Lu et al., 2016), and the crystallization of amphibole (into which Y preferentially partitions) but suppression of plagioclase crystallization (into which Eu preferentially partitions) under hydrous conditions. These element ratios, however, overlap between mineralized and subeconomic intrusions at Yulong (Fig. 10), suggesting that they have similar and relatively high oxidation and hydration states (Ballard et al., 2002; Lu et al., 2016).

Europium and Ce anomalies in apatite and titanite have also been suggested to be proxies for the oxidation state of the parent magma (Cao et al., 2012, 2015; Ding et al., 2015; Pan et al., 2016) due to the preferred substitution of trivalent Eu and Ce compared to Eu^{2+} and Ce^{4+} (titanite: REE^{3+} + (Al, Fe)$^{3+}$ = Ca^{2+} + Ti^{4+}, Green and Pearson, 1986; apatite: REE^{3+} + Si^{4+} = Ca^{2+} + P^{5+}, Sha and Chappell, 1999), with apatite and titanite crystals crystallized under higher oxidation states having relatively higher Eu_N/Eu_N^* and lower Ce_N/Ce_N^* values. However, several recent studies (e.g., Xu et al., 2015; Li et al., 2017) have shown that the Eu_N/Eu_N^* values can be misleading at times due to the compatible behavior of Eu in plagioclase. Therefore,
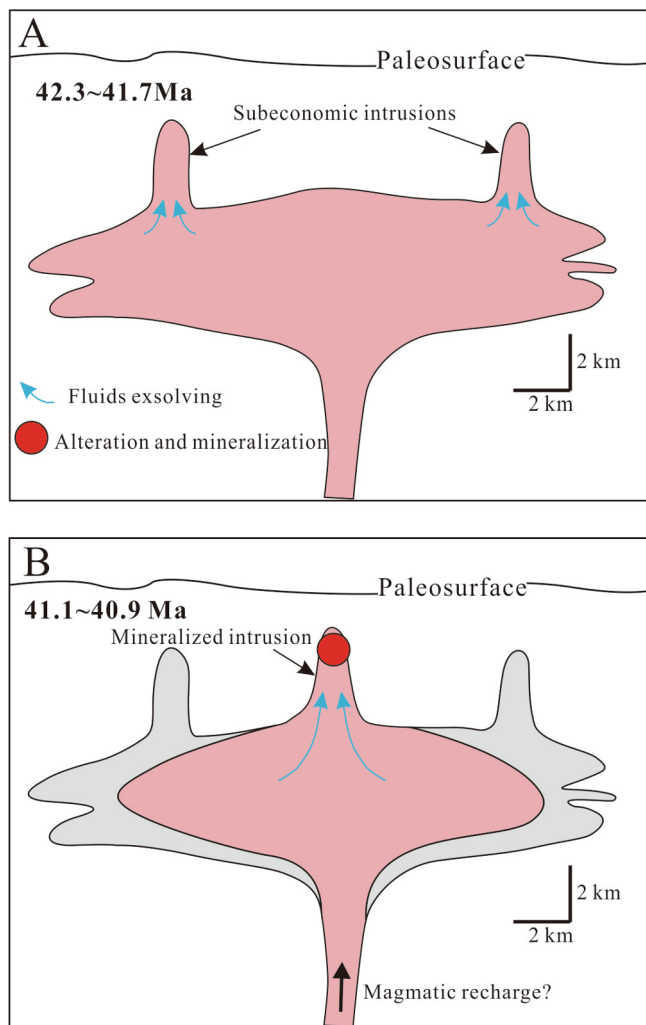
Fig. 13. Simplified model for the ore-forming process at the Yulong porphyry Cu-Mo deposit. A. Emplacement of the early, subeconomic intrusions. Minor fluid exsolution occurred during this period. B. Cooling and crystallization of the magma chamber led to a build-up of volatiles, whose sudden and voluminous release coeval with emplacement of the Yulong intrusion was triggered by an as yet unidentified process, but possibly including magmatic recharge.

in this study, the Eu_N/Eu_N^* values are not used for indicating oxidation states of the host magma. Both apatite and titanite crystals have decreasing Ce_N/Ce_N^* values with increasing La/Yb ratios, with the late, mineralized intrusion having lower Ce_N/Ce_N^* and higher La/Yb ratios (Figs. 11A and 12B). Given that La/Yb ratios increase with amphibole fractionation (Lang and Titley, 1998; Richards et al., 2001; Richards and Kerrich, 2007; Richards, 2011b), these observed negative trends may reflect increasing oxidation and hydration states through magma evolution (Rohrlach and Loucks, 2005; Chiaradia et al., 2009; Richards et al., 2013, 2018; Lee et al., 2017). Nonetheless, we note that the difference of Ce_N/Ce_N^* values is small, and therefore we consider that the subeconomic intrusions are also relatively oxidized and hydrous, as also reflected in their high zircon Eu_N/Eu_N^* and $10,000*(Eu_N/Eu_N^*)/Y$ values (Fig. 10).

Apatite SO_3 contents are affected by temperature, oxidation state and sulfur content of the melt from which the apatite crystallized (Peng et al., 1997; Parat and Holtz, 2005; Parat and Klügel, 2011). The mineralized and subeconomic intrusions in this study have very similar compositions (Fig. 8), Ti-in-zircon temperatures (Table A5; Ferry and Watson, 2007), and oxidation states (Fig. 10). We therefore consider that the apatite SO_3 contents should qualitatively reflect the sulfur content of the host magma. The SO_3 contents of apatite cores from the

mineralized (0.65 ± 0.24 wt%, n = 21) and subeconomic intrusions (0.61 ± 0.27 wt%, n = 15) are almost the same, and are both higher than the values of global porphyry Cu deposits (Richards et al., 2017, and the references therein). We therefore conclude that the parental magmas that generated the mineralized and subeconomic intrusions were both sulfur-rich.

Taken together, zircon, apatite, and titanite compositions suggest that the parental magmas to both the mineralized and subeconomic intrusions were relatively oxidized, hydrous and S-rich, and thus had the potential to produce porphyry Cu mineralization. A small increase in oxidation and hydration states is suggested by higher La/Yb and lower Ce_N/Ce_N^* values in apatites and titanites from the mineralized Yulong intrusion, possibly reflecting build-up of volatiles (Fig. 13), and late-stage fractionation or degassing effects (e.g., Mathez, 1984; Candela, 1986a; Dilles et al., 2015), but the difference is small.

5.3. Trigger(s) of ore formation

Of particular interest at Yulong is that although these intrusions have very similar compositions and ages (Figs. 7 and 8; Jiang et al., 2006; Guo et al., 2006; Wang et al., 2009, 2011), only the Yulong intrusion was intensively mineralized. Based on zircon and apatite compositions discussed above, we consider that magmatic oxidation and hydration states and sulfur contents are high throughout the intrusive suite, and these variables cannot explain the exclusive mineralization in the Yulong intrusion.

Apatite crystals from the mineralized Yulong intrusion have lower Cl and higher F contents and higher F/Cl ratios than those of the subeconomic intrusions (Fig. 11B-D). Because these intrusions were emplaced within a relatively short period of time (~1 m.y.), and probably share a common source magma chamber (Fig. 13), the distinct Cl and F contents in these intrusions is unlikely to have been caused by different magma sources. It has been shown that Cl is preferentially partitioned into the aqueous volatile phases exsolving from a magma, whereas F is preferentially retained in the melt (Candela, 1986b; Webster et al., 2009; Zhang et al., 2012); thus, fluid exsolution will result in relatively low Cl contents and high F/Cl ratios in apatite crystallized from the residual magma (Fig. 11C). Therefore the lower apatite F/Cl ratios of the subeconomic intrusions suggest that only a small amount of water had been exsolved from the source magma chamber prior to their emplacements. As a consequence, most of the water remained in the magma chamber until its sudden and voluminous release coeval with emplacement of the Yulong intrusion, which is recorded by the higher apatite F/Cl ratios. This is also consistent with its association with the most intensive hydrothermal alteration and mineralization.

The key question is what triggered extensive fluid exsolution only during the emplacement of the Yulong intrusion (Richards, 2018). It has been demonstrated that the injection of less-evolved, volatile-rich magma into an evolving magma chamber could remobilize the resident (more felsic) magma, and trigger fluid saturation and porphyry mineralization (Hattori and Keith, 2001; Tapster et al., 2016; Buret et al., 2017; Large et al., 2018). We tentatively speculate that this process may have been the case at Yulong (Fig. 13), because a few apatite crystals from the mineralized Yulong intrusion are characterized by cyclical sulfur zonation (Fig. 6E), which may be indicative of repeated magmatic recharge. However, this interpretation is not conclusive, and more work is needed to understand the trigger for ore-formation at Yulong.

6. Conclusions

Felsic porphyry intrusions in the Yulong porphyry Cu-Mo ore district were emplaced over a relatively short period of time (43.9 ± 0.6 Ma to 40.9 ± 0.3 Ma), with the mineralized Yulong intrusion emplaced at late stage of the magmatic activity (41.1 ± 0.3 Ma to 40.9 ± 0.3 Ma). Zircon and apatite compositions suggest that the

parental magmas to both the subeconomic and mineralized intrusions were relatively oxidized, hydrous and S-rich, and therefore have the potential to form porphyry-type mineralization. The fact that only the later Yulong intrusion was significantly mineralized indicates that an additional factor is required to trigger ore-formation in otherwise similarly fertile magmas. Higher mineral La/Yb ratios, and lower Cl contents and higher F/Cl ratios in apatite crystals from the mineralized intrusion, may reflect slightly higher water contents and more extensive devolatilization of the source magma chamber immediately prior to or during emplacement of these magmas. These changes may reflect cooling and crystallization in the underlying magma chamber, leading to a build-up of volatiles whose sudden and voluminous release coeval with emplacement of the Yulong intrusion was triggered by an as yet unidentified process, but possibly involving magmatic recharge.

Acknowledgements

Declaration of interest statement

We declare that we do not have any commercial or associative interest that represents a conflict of interest in connection with the work submitted.

Appendix A

A.1. Whole rock major and trace element analyses

Whole-rock major element compositions were determined using an Axios PW4400 X-ray fluorescence spectrometer (XRF) at ALS Chemex, Guangzhou, China, using fused lithum-tetraborate glass pellets. The analytical accuracy is better than 5 relative %. Trace element compositions were analyzed using a PerkinElmer DRC-e ICP-MS at SKLODG, IGCAS. Fifty milligrams of powdered sample were dissolved in high-pressure Teflon bombs with a HF/HNO_3 mixture for 2 days at 190 °C. Rhodium was added into the dissolved samples and was analyzed as an internal standard to monitor signal drift during counting. Detailed analytical methods are given by Qi et al. (2000). The analytical accuracy is generally better than 10 relative %.

A.2. Electron microprobe analyses and CL/BSE imaging

Cathodoluminescence (CL) and back-scattered electron (BSE) images of zircon, apatite, and titanite were obtained at the State Key Laboratory of Ore deposit Geochemistry, Institute of Geochemistry, Chinese Academy of Sciences. Major element compositions of all selected apatite and most titanite grains were obtained on a JEOL JXA-8230 electron microprobe at Shandong Bureau Testing Center of China Metallurgical Geology Bureau (Jinan), with operating conditions of 25 kV accelerating voltage, 10 nA beam current, and 5 μm beam diameter. All data were corrected based on the ZAF procedure. For apatite,

peak/background counting times were 20 s/10 s for F and Fe, and 10 s/5s for the other elements. Standards used for calibrating elements include phlogopite (F), jadeite (Na and Si), diopside (Mg), garnet (Al), olivine (Fe), rhodonite (Mn), apatite (Ca and P), anhydrite (S), barite (Ba), sanidine (K) and celestite (Sr). Detection limits were ~ 100 ppm for Na, Mg, Al, K and Cl, 100–300 ppm for Fe, Mn, Ca and S, 300–400 ppm for F and Ba, and 500–600 ppm for Sr. For titanite, peak/background counting times were 8 s/4s for F, 10 s/5s for Mg, Al, Si, Ti, Ca, P, and Cl, 20 s/10 s for Mn, Fe, S and Y, and 40 s/20 s for Ce and Sr. The standards used for calibrating elements include phlogopite (F), jadeite (Si), diopside (Mg), garnet (Al), olivine (Fe), rhodonite (Mn), apatite (Ca and P), anhydrite (S), rutile (Ti), monazite (Ce) and celestite (Sr). Detection limits were ~ 100 ppm for Mg, Al, Si, Ca, Sr, Y, S and Cl, 100–200 ppm for Fe, Mn and P, and 200–350 ppm for F, Ti and Ce.

Major element compositions of titanite crystals extracted from sample YL1648 and ZK1007-671 were obtained on an EPMA-1600 electron microprobe using wave-length-dispersive spectrometers (WDS) at the State Key Laboratory of Ore Deposit Geochemistry (SKLODG), Institute of Geochemistry, Chinese Academy of Sciences (IGCAS). The following natural minerals were used as standards: amphibole (Na, K, Mg, Al, Si, Ca, Mn and Fe), apatite (F), tugtupite (Cl) and rutile (Ti). The analytical conditions were 25 kV accelerating voltage, 10 nA beam current, and 10 μm beam diameter. Counting/background times of 20 s/10 s were used for most elements, except 40 s/20 s for F, and 10 s/5s for P and Ca at their characteristic X-ray line.

A.3. Secondary ion mass spectrometry (SIMS) zircon U-Pb dating

In-Situ secondary ion mass spectrometry (SIMS) zircon U-Pb dating was conducted using a Cameca 1280HR SIMS. Grains of Qinghu zircon (159.5 ± 0.2 Ma, 2σ; Li et al., 2013) were used as external standards, and were mounted in the epoxy disc together with sample zircons. The epoxy disc was polished to half thickness of the zircon grains and then coated with gold. The zircon crystals were sputtered by an O^{2-} primary ion beam with an intensity of ca. 8 nA and a accelerated voltage of −13 kV. A spot size of ca. 20 μm × 30 μm was applied. U-Pb isotopic compositions were calibrated against the Qinghu zircon standard (Li et al., 2013). Common Pb was corrected using measured non-radiogenic ^{204}Pb and an average present day crustal Pb compositions (Stacey and Kramers, 1975). Detailed analytical procedures are described in Li et al. (2009). Uncertainties for individual analyses are reported at 1σ error, and plotted at 2σ error using Isoplot/Ex_ver3 software (Ludwig, 2003).

A.4. Laser-ablation ICP-MS zircon U-Pb dating

In-situ LA-ICP-MS uranium and lead isotopic analyses of zircon grains were conducted using a GeoLasPro 193 nm ArF excimer laser equipped with Agilent 7900 ICP-MS. A laser spot size of 32 μm with repetition rate of 6 Hz was used during the analyses. Each analysis included a background acquisition of about 20 s (gas blank) followed by 50 s of data acquisition from the sample. Helium was used as the carrier gas, and argon was used as the makeup gas. They were mixed via a T-connector before entering the ICP-MS. Off-line selection and integration of background and analysis signals, time-drift correction, and quantitative calibrations were performed by ICPMSDataCal software (Liu et al., 2008, 2010). Zircon 91,500 and GJ-1 were used as external standards for U-Pb dating. Preferred U-Pb isotopic ratios of Zircon 91,500 are from Wiedenbeck et al. (1995). Uncertainty of preferred values for the external standard Zircon 91,500 was propagated through the ultimate results of the samples. NIST 610 was used as external standard for trace element calibrations, and was analyzed twice every 10 analyses. Concordia diagrams and weighted mean calculations were made using Isoplot software (Ludwig, 2003).

A.5. LA-ICP-MS trace element analysis of zircon, titanite and apatite

LA-ICP-MS trace element analysis of zircon, titanite, and apatite were conducted using a GeoLasPro 193 nm ArF excimer laser equipped with Agilent 7900 ICP-MS at SKLODG, IGCAS, with laser spot size of 32 μm and pulse rate of 6–8 Hz. NIST glasses 610 and 612 were used as external calibration standards. All analyses were recorded for 90 s including approximately 20 s gas blank followed by 50 s data acquisition. Off-line selection and integration of background and analyte signals, time-drift correction, and quantitative calibrations were performed using ICPMS DataCal software (Liu et al., 2008, 2010). Calcium, whose concentration was obtained independently by EMPA analysis on the same spot, was used as an internal standard for off-line LA-ICP-MS calibration of both titanite and apatite. The analytical results of the standard NIST 610 and 612 are consistent with the reference values (http://georem.mpch-mainz.gwdg.de/sample_query_pref.asp) within 10% for most trace elements. For zircons that were dated by LA-ICP-MS, trace element compositions were obtained simultaneously with U-Pb isotopic compositions using the procedures presented above. For zircons that were dated by SIMS, the trace element compositions were obtained by LA-ICP-MS analysis on the spots that were previously used for SIMS dating. The analytical procedures are similar to those used for apatite and titanite, except for using ^{29}Si as the internal standard element.

Appendix B. Supplementary material

Supplementary data to this article can be found online at https://doi.org/10.1016/j.jseaes.2019.02.008.

References

Aleinikoff, J.N., Wintsch, R.P., Fanning, C.M., Dorais, M.J., 2002. U-Pb geochronology of zircon and polygenetic titanite from the Glastonbury Complex, Connecticut, USA: an integrated SEM, EMPA, TIMS, and SHRIMP study. Chem. Geol. 188, 125–147.

Ballard, J.R., Palin, M.J., Campbell, I.H., 2002. Relative oxidation states of magmas inferred from Ce(IV)/Ce(III) in zircon: application to porphyry copper deposits of northern Chile. Contrib. Miner. Petrol. 144, 347–364.

Belousova, E., Griffin, W., O'Reilly, S.Y., Fisher, N., 2002. Igneous zircon: trace element composition as an indicator of source rock type. Contrib. Miner. Petrol. 143, 602–622.

Bi, X.W., Hu, R.Z., Ye, Z.J., Shao, S.X., 1999. Study on the relation between the A-type granite and Cu ore mineralization: evidence from the Machangqing copper deposit. Sci. China (Ser. D) 29, 489–495 (in Chinese).

Bi, X.W., Cornell, D.H., Hu, R.Z., 2002. REE composition of primary and altered feldspar from the mineralized alteration zone of alkaline intrusive rocks, western Yunnan Province, China. Ore Geol. Rev. 19, 69–78.

Bi, X.W., Hu, R.Z., Cornell, D.H., 2004. The alkaline porphyry associated Yao'an gold deposit, Yunnan, China: rare earth element and stable isotope evidence for magmatic-hydrothermal ore formation. Miner. Deposita 39, 21–30.

Bi, X.W., Hu, R.Z., Peng, J.T., Wu, K.X., Su, W.C., Zhan, X.Z., 2005. Geochemical characteristics of the Yao'an and Machangqing alkaline[HYPHEN]rich intrusions. Acta Petrol. Sin. 21, 113–124 (in Chinese with English abstract).

Bi, X.W., Hu, R.Z., Hanley, J.J., Mungall, J.E., Peng, J., Shang, L., Wu, K.X., Yan, S., Li, H.L., Hu, X.Y., 2009. Crystallization conditions (T, P, fO2) from mineral chemistry of Cu- and Au-mineralized alkaline intrusions in the Red River-Jinshajiang alkaline igneous belt, western Yunnan Province, China. Mineral. Petrol. 96, 43–58.

Boudreau, A.E., Mccallum, I.S., 1989. Investigations of the Stillwater Complex: Part V. Apatites as indicators of evolving fluid composition. Contrib. Miner. Petrol. 102, 138–153.

Bouzari, F., Hart, C.J.R., Barker, S., Bissig, T., 2009. Porphyry indicator minerals (PIMs): exploration for concealed deposits in southcentral British Columbia (NTS 092I/06, 093A/12, 093N/01, /14). in Geoscience BC Summary of Activities 2009, Geoscience BC, Report 2010-1, pp. 25–32.

Boyce, J.W., Hervig, R.L., 2009. Apatite as a monitor of late-stage magmatic processes at Volcán Irazú, Costa Rica. Contrib. Miner. Petrol. 157, 135–145.

Buret, Y., Wotzlaw, J.-F., Roozen, S., Guillong, M., Quadt, A.V., Heinrich, C.A., 2017. Zircon petrochronological evidence for a plutonic-volcanic connection in porphyry copper deposits. Geology 45, 623–626.

Burnham, C.W., 1979. Magmas and hydrothermal fluids. In: Barnes, H.L. (Ed.), Geochemistry of Hydrothermal Ore Deposits, second ed. John Wiley and Sons, New York, pp. 71–136.

Candela, P.A., 1986a. The evolution of aqueous vapor from silicate melts: Effect on oxygen fugacity. Geochim. Cosmochim. Acta 50, 1205–1211.

Candela, P.A., 1986b. Toward a thermodynamic model for the halogens in magmatic systems: An application to melt-vapor-apatite equilibria*. Chem. Geol. 57, 289–301.

Candela, P.A., 1992. Controls on ore metal ratios in granite-related ore systems: an experimental and computational approach. Trans. Royal Soc. Edinburgh Earth Sci. 83,

317–326.

Castillo, P.R., Janney, P.E., Solidum, R.U., 1999. Petrology and geochemistry of Camiguin Island, southern Philippines: Insights to the source of adakites and other lavas in a complex arc setting. Contrib. Miner. Petrol. 134, 33–51.

Cao, M.J., Li, G.M., Qin, K.Z., Seitmuratova, E.Y., Liu, Y.S., 2012. Major and trace element characteristics of apatites in granitoids from Central Kazakhstan: Implications for petrogenesis and mineralization. Resour. Geol. 62, 63–83.

Cao, M.J., Qin, K.Z., Li, G.M., Yang, Y.H., Evans, N.J., Zhang, R., Jin, L.Y., 2014. Magmatic process recorded in plagioclase at the Baogutu reduced porphyry Cu deposit, western Junggar, NW-China. J. Asian Earth Sci. 82, 136–150.

Cao, M.J., Qin, K.Z., Li, G.M., Evans, N.J., Jin, L.Y., 2015. In situ LA-(MC)-ICP-MS trace element and Nd isotopic compositions and genesis of polygenetic titanite from the Baogutu reduced porphyry Cu deposit, Western Junggar, NW China. Ore Geol. Rev. 65, 940–954.

Chang, J., Li, J.W., Selby, D., Liu, J.C., Deng, X.D., 2017. Geological and chronological constraints on the long-lived Eocene Yulong porphyry Cu-Mo deposit, eastern Tibet, China: implications for lifespan of magmatic-hydrothermal processes forming giant and supergiant porphyry Cu deposits. Econ. Geol. 112, 1719–1746.

Chen, M.H., Bagas, L., Liao, X., Zhang, Z.Q., Li, Q.L., 2019. Hydrothermal apatite SIMS Th-Pb dating: Constraints on the timing of low-temperature hydrothermal Au deposits in Nibao, SW China. Lithos 324–325, 418–428.

Chiaradia, M., Merino, D., Spikings, R., 2009. Rapid transition to long-lived deep crustal magmatic maturation and the formation of giant porphyry-related mineralization (Yanacocha, Peru). Earth Planet. Sci. Lett. 288, 505–515.

Corfu, F., Hanchar, J.M., Hoskin, P.W.O., Kinny, P., 2003. Atlas of zircon textures. Rev. Mineral. 53, 469–500.

Deng, J., Wang, Q.F., Li, G.J., Hou, Z.Q., Jiang, C.Z., Danyushevsky, L., 2015. Geology and genesis of the giant Beiya porphyry–skarn gold deposit, northwestern Yangtze Block, China. Ore Geol. Rev. 70, 457–485.

Dilles, J.H., Kent, A.J.R., Wooden, J.L., Tosdal, R.M., Koleszar, A., Lee, R.G., Farmer, L.P., 2015. Zircon compositional evidence for sulfur-degassing from ore-forming arc magmas. Econ. Geol. 110, 241–251.

Ding, T., Ma, D., Lu, J., Zhang, R., 2015. Apatite in granitoids related to polymetallic mineral deposits in southeastern Hunan Province, Shi-Hang zone, China: Implications for petrogenesis and metallogenesis. Ore Geol. Rev. 69, 104–117.

Duan, D.F., Jiang, S.Y., 2018. Using apatite to discriminate synchronous ore-associated and barren granitoid rocks: A case study from the Edong metallogenic district, South China. Lithos 310–311, 369–380.

Ferry, J.M., Watson, E.B., 2007. New thermodynamic models and revised calibrations for the Ti-in-zircon and Zr-in-rutile thermometers. Contrib. Miner. Petrol. 154, 429–437.

Frost, B.R., Chamberlain, K.R., Schumacher, J.C., 2000. Sphene (titanite): phase relations and role as a geochronometer. Chem. Geol. 172, 131–148.

Fu, Y., Sun, X., Zhou, H., Lin, H., Yang, T., 2016. In-situ LA–ICP–MS U-Pb geochronology and trace elements analysis of polygenetic titanite from the giant Beiya gold–polymetallic deposit in Yunnan Province, Southwest China. Ore Geol. Rev. 77, 43–56.

Green, T.H., Pearson, N.J., 1986. Rare-earth element partitioning between sphene and coexisting silicate liquid at high pressure and temperature. Chem. Geol. 55, 105–119.

Gu, X.X., Tang, J.X., Wang, C.S., Chen, J.P., He, B.B., 2003. Himalayan magmatism and porphyry copper–molybdenum mineralization in the Yulong ore belt, East Tibet. Mineral. Petrol. 78, 1–20.

Guo, L.G., Liu, Y.P., Xu, W., Zhang, X.C., Qin, K.Z., Li, T.S., Shi, Y.R., 2006. Constraints to the mineralization age of the Yulong porphyry copper deposit from SHRIMP U-Pb zircon data in Tibet. Acta Petrologica Sinica 22, 1009–1016 (in Chinese with English abstract).

Hattori, K.H., Keith, J.D., 2001. Contribution of mafic melt to porphyry copper mineralization: evidence from Mount Pinatubo, Philippines, and Bingham Canyon, Utah, USA. Miner. Deposita 36, 799–806.

He, W.Y., Mo, X.X., He, Z.H., White, N.C., Chen, J.B., Yang, K.H., Wang, R., Yu, X.H., Dong, G.C., Huang, X.F., 2015. The geology and mineralogy of the Beiya skarn gold deposit in Yunnan, Southwest China. Econ. Geol. 110, 1625–1641.

Hou, Z.Q., Ma, H., Zaw, K., Zhang, Y.Q., Wang, M.J., Wang, Z., Pan, G.T., Tang, R.L., 2003. The Himalayan Yulong porphyry copper belt: Product of large-scale strike-slip faulting in eastern Tibet. Econ. Geol. 98, 125–145.

Hou, Z.Q., Zeng, P.S., Gao, Y.F., Du, A.D., Fu, D.M., 2006. Himalayan Cu–Mo–Au mineralization in the eastern Indo-Asian collision zone: constraints from Re–Os dating of molybdenite. Miner. Deposita 41, 33–45.

Hu, R.Z., Burnard, P.G., Turner, G., Bi, X.W., 1998. Helium and argon systematics in fluid inclusions of Machangqing copper deposit inwest Yunnan province. China. Chem. Geol. 146, 55–63.

Hu, R.Z., Bi, X.W., Turner, G., Burnard, P.G., 1999. He and Ar isotopic geochemistry of the ore-forming fluids of the Ailaoshan Au ore belt. Sci. China (Ser. D) 29, 321–330 (in Chinese).

Hu, R.Z., Burnard, P.G., Bi, X.W., Zhou, M.F., Pen, J.T., Su, W.C., Wu, K.X., 2004. Helium and argon isotope geochemistry of alkaline intrusion-associated gold and copper deposits along the Red River-Jinshajiang fault belt, SW China. Chem. Geol. 203, 305–317.

Jiang, Y.H., Jiang, S.Y., Ling, H.F., Dai, B.Z., 2006. Low-degree melting of a metasomatized lithospheric mantle for the origin of Cenozoic Yulong monzogranite-porphyry, east Tibet: Geochemical and Sr–Nd–Pb–Hf isotopic constraints. Earth Planet. Sci. Lett. 241, 617–633.

Jugo, P.J., Luth, R.W., Richards, J.P., 2005. Experimental data on the speciation of sulfur as a function of oxygen fugacity in basaltic melts. Geochim. Cosmochim. Acta 69, 497–503.

Lang, J.R., Titley, S.R., 1998. Isotopic and geochemical characteristics of Laramide magmatic systems in Arizona and implications for the genesis of porphyry copper deposits. Econ. Geol. 93, 138–170.

Large, S.J.E., Quadt, A.v., Wotzlaw, J.-F., Guillong, M., Heinrich, C.A., 2018. Magma evolution leading to porphyry Au-Cu mineralization at the Ok Tedi Deposit, Papua New Guinea: Trace element geochemistry and high-precision geochronology of igneous zircon. Econ. Geol. 113, 39–61.

Lee, R.G., Dilles, J.H., Tosdal, R.M., Wooden, J.L., Mazdab, F.K., 2017. Magmatic evolution of granodiorite intrusions at the El Salvador Porphyry copper deposit, chile, based on trace element composition and U/Pb age of zircons. Econ. Geol. 112, 245–273.

Leech, M.L., Singh, S., Jain, A.K., Klemperer, S.L., Manickavasagam, R.M., 2005. The onset of India-Asia continental collision: Early, steep subduction required by the timing of UHP metamorphism in the western Himalaya. Earth Planet. Sci. Lett. 234, 83–97.

Li, C., Hao, X., Liu, J., Ling, M., Ding, X., Zhang, H., Sun, W., 2017. The formation of Luoboling porphyry Cu–Mo deposit: Constraints from zircon and apatite. Lithos 272–273, 291–308.

Li, J., Qin, K., Li, G., Cao, M., Xiao, B., Chen, L., Zhao, J., Evans, N.J., McInnes, B.I.A., 2012. Petrogenesis and thermal history of the Yulong porphyry copper deposit, Eastern Tibet: insights from U-Pb and U-Th/He dating, and zircon Hf isotope and trace element analysis. Mineral. Petrol. 105, 201–221.

Liaghat, S., Tosdal, R., 2008. Apatite chemical composition and textures as a probe into magmatic conditions at Galore Creek porphyry copper-gold deposit, British Columbia. Geochm. Cosmochim. Acta 72, A550.

Liang, H.-Y., Campbell, I.H., Allen, C., Sun, W.-D., Liu, C.-Q., Yu, H.-X., Xie, Y.-W., Zhang, Y.-Q., 2006. Zircon Ce^{4+}/Ce^{3+} ratios and ages for Yulong ore-bearing porphyries in eastern Tibet. Miner. Deposita 41, 152–159.

Lin, B., Wang, L., Tang, J., Song, Y., Cao, H., Baker, M.J., Zhang, L., Zhou, X., 2018. Geology, geochronology, geochemical characteristics and origin of Baomai porphyry Cu (Mo) deposit, Yulong Belt, Tibet. Ore Geol. Rev. 92, 186–204.

Loader, M.A., Wilkinson, J.J., Armstrong, R., 2017. The effect of titanite crystallisation on Eu and Ce anomalies in zircon and its implications for the assessment of porphyry Cu deposit fertility. Earth Planet. Sci. Lett. 472, 107–119.

Longo, A.A., Dilles, J.H., Grunder, A.L., Duncan, R., 2010. Evolution of calc-alkaline volcanism and associated hydrothermal gold deposits at Yanacocha, Peru. Econ. Geol. 105, 1191–1241.

Loucks, R.R., 2014. Distinctive composition of copper-ore-forming arc magmas. Aust. J. Earth Sci. 61, 5–16.

Lu, Y.J., Loucks, R.R., Fiorentini, M., Mccuaig, T.C., Evans, N., Yang, Z., Hou, Z., Kirkland, C., Parra-Avila, L.A., Kobussen, A., 2016. Zircon compositions as a pathfinder for porphyry Cu ± Mo ± Au deposits. Soc. Economic Geol., Spec. Publ. 19, 329–347.

Mao, M., Rukhlov, A.S., Rowins, S.M., Spence, J., Coogan, L.A., 2016. Apatite trace element compositions: a robust new tool for mineral exploration. Econ. Geol. 111, 1187–1222.

Mathez, E.A., 1984. Influence of degassing on oxidation-states of basaltic magmas. Nature 310, 371–375.

Metrich, N., Clocchiatti, R., 1996. Sulfur abundance and its speciation in oxidized alkaline melts. Geochim. Cosmochim. Acta 60, 4151–4160.

Miles, A.J., Graham, C.M., Hawkesworth, C.J., Gillespie, M.R., Hinton, R.W., Bromiley, G.D., 2014. Apatite: A new redox proxy for silicic magmas? Geochim. Cosmochim. Acta 132, 101–119.

Mo, X., Hou, Z., Niu, Y., Dong, G., Qu, X., Zhao, Z., Yang, Z., 2007. Mantle contributions to crustal thickening during continental collision: Evidence from Cenozoic igneous rocks in southern Tibet. Lithos 96, 225–242.

Mungall, J.E., 2002. Roasting the mantle: Slab melting and the genesis of major Au and Au-rich Cu deposits. Geology 30, 915–918.

Pan, L.C., Hu, R.Z., Wang, X.S., Bi, X.W., Zhu, J.J., Li, C., 2016. Apatite trace element and halogen compositions as petrogenetic-metallogenic indicators: Examples from four granite plutons in the Sanjiang region, SW China. Lithos 254–255, 118–130.

Pan, Y., Fleet, M.E., 2002. Compositions of the apatite-group minerals: substitution mechanisms and controlling factors. Rev. Mineral. Geochem. 48, 13–49.

Parat, F., Holtz, F., 2005. Sulfur partition coefficient between apatite and rhyolite: the role of bulk S content. Contrib. Miner. Petrol. 150, 643–651.

Parat, F., Klügel, A., 2011. S-rich apatite-hosted glass inclusions in xenoliths from La Palma: constraints on the volatile partitioning in evolved alkaline magmas. Contrib. Miner. Petrol. 162, 463–478.

Peng, G., Luhr, J.F., Mcgee, J.J., 1997. Factors controlling sulfur concentrations in volcanic apatite. Am. Mineral. 82, 1210–1224.

Richards, J.P., 2003. Tectono-magmatic precursors for porphyry Cu(Mo-Au) deposit formation. Econ. Geol. 98, 1515–1533.

Richards, J.P., 2011a. Magmatic to hydrothermal metal fluxes in convergent and collided margins. Ore Geol. Rev. 40, 1–26.

Richards, J.P., 2011b. High Sr/Y arc magmas and porphyry Cu ± Mo ± Au deposits: Just add water. Econ. Geol. 106, 1075–1081.

Richards, J.P., 2015. The oxidation state, and sulfur and Cu contents of arc magmas: implications for metallogeny. Lithos 233, 27–45.

Richards, J.P., 2018. A shake-up in the porphyry world? Econ. Geol. 113, 1225–1233.

Richards, J.P., Kerrich, R., 2007. Special paper: adakite-like rocks: their diverse origins and questionable role in metallogenesis. Econ. Geol. 102, 537–576.

Richards, J.P., Jourdan, F., Creaser, R.A., Maldonado, G., DuFrane, S.A., 2013. Geology, geochemistry, geochronology, and economic potential of Neogene volcanic rocks in the Laguna Pedernal and Salar de Aguas Calientes segments of the Archibarca lineament, northwest Argentina. J. Volcanol. Geoth. Res. 258, 47–73.

Richards, J.P., Boyce, A.J., Pringle, M.S., 2001. Geologic evolution of the Escondida Area, Northern Chile: A model for spatial and temporal localization of porphyry Cu mineralization. Econ. Geol. 96, 126–131.

Richards, J.P., López, G.P., Zhu, J.J., Creaser, R.A., Locock, A.J., Mumin, A.H., 2017. Contrasting tectonic settings and sulfur contents of magmas associated with cretaceous porphyry Cu ± Mo ± Au and intrusion-related iron oxide Cu-Au deposits in northern chile. Econ. Geol. 112, 295–318.

Richards, J.P., Razavi, A.M., Spell, T.L., Locock, A., Sholeh, A., Aghazadeh, M., 2018. Magmatic evolution and porphyry–epithermal mineralization in the Taftan volcanic complex, southeastern Iran. Ore Geol. Rev. 95, 258–279.

Rohrlach, B.D., Loucks, R.R., 2005. Multi-million-year cyclic ramp-up of volatiles in a lower-crustal magma reservoir trapped below the Tampakan copper–gold deposit by Mio–Pliocene crustal compression in the southern Philippines. In: Porter, T.M. (Ed.), Super Porphyry Copper & Gold Deposits—A Global Perspective. PCG Publishing, Adelaide, South Austria, pp. 369–407.

Romick, J.D., Kay, S.M., Kay, R.W., 1992. The influence of amphibole fractionation on the evolution of calc-alkaline andesite and dacite tephra from the central Aleutians, Alaska. Contrib. Miner. Petrol. 112, 101–118.

Rooney, T.O., Franceschi, P., Hall, C.M., 2011. Water-saturated magmas in the Panama Canal region: A precursor to adakite-like magma generation? Contrib. Miner. Petrol. 161, 373–388.

Seedorff, E., Dilles, J.H., Proffett, J.M., Einaudi, M.T., Zurcher, L., Stavast, W.J.A., Johnson, D.A., Barton, M.D., 2005. Porphyry deposits: Characteristics and origin of hypogene features. Economic Geology 100th Anniversary Volume 251–298.

Sha, L.K., Chappell, B.W., 1999. Apatite chemical composition by electron microprobe and laser-ablation inductively coupled plasma spectrometry, as a probe into granite petrogenesis. Geochim. Cosmochim. Acta 63, 3861–3881.

Sillitoe, R.H., 2010. Porphyry copper systems. Econ. Geol. 105, 3–41.

Streck, M.J., Dilles, J.H., 1998. Sulfur evolution of oxidized arc magmas as recorded in apatite from a porphyry copper batholith. Geology 26, 523–526.

Sun, S.S., McDonough, W.F., 1989. Chemical and isotopic systematics of oceanic basalts: implications for mantle composition and processes. Geol. Soc. London Spec. Publ. 42, 313–345.

Tang, J.X., Wang, C.H., Qu, W.J., Du, A.D., Ying, L.J., Gao, Y.M., 2009. Re-Os isotopic dating of molybdenite from the Yulong porphyry coppe rmolybdenum deposit in Tibet and its metallogenic significance: Rock and Mineral Analysis 28, 215–218 (in Chinese with English abstract).

Tang, R.L., Luo, H.S., 1995. The Geology of Yulong Porphyry Copper (molybdenum) Ore Belt, Xizang (Tibet). Geological Publishing House, Beijing, pp. 320 (in Chinese).

Tapster, S., Condon, D.J., Naden, J., Noble, S.R., Petterson, M.G., Roberts, N.M.W., Saunders, A.D., Smith, D.J., 2016. Rapid thermal rejuvenation of high-crystallinity magma linked to porphyry copper deposit formation; evidence from the Koloula Porphyry Prospect, Solomon Islands. Earth Planet. Sci. Lett. 442, 206–217.

Tibet Yulong Copper Co., Ltd., 2009, Yulong Copper Polymetallic Deposit Exploration Report. Jomda County, Tibet.

Tiepolo, M., Oberti, R., Vannucci, R., 2002. Trace-element incorporation in titanite: constraints from experimentally determined solid/liquid partition coefficients. Chem. Geol. 191, 105–119.

Wang, C.H., Tang, J.X., Chen, J.P., Hao, J.H., Gao, Y.M., Liu, Y.W., Fan, T., Zhang, Q.Z., Ying, L.J., Chen, Z.J., 2009. Chronological research of Yulong copper-molybdenum porphyry deposit. Acta Geologic Sinica 83, 1445–1455 (in Chinese with English abstract).

Wang, C.H., Tang, J.X., Hou, K.J., Gao, Y.M., Chen, J.P., Hao, J.H., Ying, L.J., Zhang, Q.Z., Liu, Y.W., Fan, T., 2011. Hf isotopic characteristics of Yulong copper-molybdenum porphyry deposit in Tibet and their geological significance. Mineral Deposits 30, 292–304 (in Chinese with English abstract).

Wang, J.H., Yin, A., Harrison, T.M., Grove, M., Zhang, Y.Q., Xie, G.H., 2001. A tectonic model for Cenozoic igneous activities in the eastern Indo-Asian collision zone. Earth Planet. Sci. Lett. 188, 123–133.

Webster, J.D., Piccoli, P.M., 2015. Magmatic apatite: a powerful, yet deceptive. Mineral. Elements 11, 177–182.

Webster, J.D., Tappen, C.M., Mandeville, C.W., 2009. Partitioning behavior of chlorine and fluorine in the system apatite–melt–fluid. II: Felsic silicate systems at 200 MPa. Geochim. Cosmochim. Acta 73, 559–581.

Winchester, J.A., Floyd, P.A., 1977. Geochemical discrimination of different magma series and their differentiation products using immobile elements. Chem. Geol. 20, 325–343.

Xu, L., Bi, X., Hu, R., Qi, Y., Tang, Y., Wang, X., Zhu, J., 2016. Redox states and genesis of magmas associated with intra-continental porphyry Cu–Au mineralization within the Jinshajiang-Red River alkaline igneous belt, SW China. Ore Geol. Rev. 73, 330–345.

Xu, L., Bi, X., Hu, R., Tang, Y., Wang, X., Xu, Y., 2015. LA-ICP-MS mineral chemistry of titanite and the geological implications for exploration of porphyry Cu deposits in the Jinshajiang – Red River alkaline igneous belt, SW China. Mineral. Petrol. 109, 181–200.

Xu, L., Bi, X., Hu, R., Zhang, X., Su, W., Qu, W., Hu, Z., Tang, Y., 2012. Relationships between porphyry Cu–Mo mineralization in the Jinshajiang-Red River metallogenic belt and tectonic activity: Constraints from zircon U-Pb and molybdenite Re–Os geochronology. Ore Geol. Rev. 48, 460–473.

Yang, J.-H., Kang, L.-F., Peng, J.-T., Zhong, H., Gao, J.-F., Liu, L., 2018. In-situ elemental and isotopic compositions of apatite and zircon from the Shuikoushan and Xihuashan granitic plutons: Implication for Jurassic granitoid-related Cu-Pb-Zn and W mineralization in the Nanling Range, South China. Ore Geol. Rev. 93, 382–403.

Yang, Z., Hou, Z., Xu, J., Bian, X., Wang, G., Yang, Z., Tian, S., Liu, Y., Wang, Z., 2014. Geology and origin of the post-collisional Narigongma porphyry Cu–Mo deposit, southern Qinghai, Tibet. Gondwana Res. 26, 536–556.

Yin, A., Harrison, T.M., 2000. Geologic evolution of the Himalayan-Tibetan Orogen. Annu. Rev. Earth Planet. Sci. 28, 211–280.

Zhang, C., Holtz, F., Ma, C., Wolff, P.E., Li, X., 2012. Tracing the evolution and distribution of F and Cl in plutonic systems from volatile-bearing minerals: a case study from the Liujiawa pluton (Dabie orogen, China). Contrib. Miner. Petrol. 164, 859–879.

Zhang, Y., Xie, Y., 1997. Geochronology of Ailaoshan-Jinshajiang alkali-rich intrusive rocks and their Sr and Nd isotopic characteristics. Sci. China Earth Sci. 40, 524–529.

Zhang, Y.Q., Xie, Y.W., Qiu, H.N., Li, X.H., Chung, S.L., 1998. Shoshonitic series: Geochemical characteristics of elements for ore-bearing porphyry from Yulong copper ore belt in eastern Tibet. Earth Sci.-J. China Univ. Geosci. 23, 557–561 (in Chinese with English abstract).

Qi, L., Hu, J., Gregoire, D.C., 2000. Determination of trace elements in granites by inductively coupled plasma mass spectrometry. Talanta 51, 507–513.

Li, X.H., Liu, Y., Li, Q.L., Guo, C.H., Chamberlain, K.R., 2009. Precise determination of Phanerozoic zircon Pb/Pb age by multicollector SIMS without external standardization. Geochem. Geophys. Geosyst. 10, Q04010.

Li, X., Tang, G., Gong, B., Yang, Y., Hou, K., Hu, Z., Li, Q., Liu, Y., Li, W.X., 2013. Qinghu

zircon: A working reference for microbeam analysis of U-Pb age and Hf and O isotopes. Chin. Sci. Bull. 58, 4647–4654.

Liu, Y., Hu, Z., Gao, S., Günther, D., Xu, J., Gao, C., Chen, H., 2008. In-situ analysis of major and trace elements of anhydrous minerals by LA-ICP-MS without applying an internal standard. Chem. Geol. 257, 34–43.

Liu, Y., Gao, S., Hu, Z., Gao, C., Zong, K., Wang, D., 2010. Continental and oceanic crust recycling-induced melt-peridotite interactions in the trans-north China Orogen: U-Pb dating, Hf isotopes and trace elements in zircons from mantle xenoliths. J. Petrol. 51, 537–571.

Ludwig, K.R., 2003. User's manual for Isoplot 3.0: A geochronological toolkit for microsoft excel. Berkeley Geochronology Center.

Stacey, J., Kramers, J., 1975. Approximation of terrestrial lead isotope evolution by a two-stage model. Earth Planet. Sci. Lett. 26, 207–221.

Wiedenbeck, M., Allé, P., Corfu, F., Griffin, W.L., Meier, M., Oberli, F., Quadt, A.V., Roddick, J.C., Spiegel, W., 1995. Three natural zircon standards for U-Th-Pb, Lu-Hf, trace element and REE analyses. Geostand. Geoanal. Res. 19, 1–23.